Journal of Computational Physics 230 (2011) 159–184

Contents lists available at ScienceDirect

Journal of Computational Physics

journal homepage: www.elsevier.com/locate/jcp

Reduced-order modeling of transonic flows around an airfoil submitted to small deformations

Rémi Bourguet [a,*], Marianna Braza [b], Alain Dervieux [c]

[a] Massachusetts Institute of Technology, 77 Massachusetts Avenue, Cambridge, MA 02139-4307, USA
[b] Institut de Mécanique des Fluides de Toulouse, 6 Allée du Professeur C. Soula, Toulouse 31400, France
[c] Institut National de Recherche en Informatique et en Automatique, 2004 Route des Lucioles – BP 93, Sophia-Antipolis 06902, France

ARTICLE INFO

Article history:
Received 15 September 2009
Received in revised form 11 May 2010
Accepted 14 September 2010
Available online 19 September 2010

Keywords:
Reduced-order modeling
Navier–Stokes equations
Hadamard formulation
Proper Orthogonal Decomposition
Transonic regime
Shape deformation

ABSTRACT

A reduced-order model (ROM) is developed for the prediction of unsteady transonic flows past an airfoil submitted to small deformations, at moderate Reynolds number. Considering a suitable state formulation as well as a consistent inner product, the Galerkin projection of the compressible flow Navier–Stokes equations, the high-fidelity (HF) model, onto a low-dimensional basis determined by Proper Orthogonal Decomposition (POD), leads to a polynomial quadratic ODE system relevant to the prediction of main flow features. A fictitious domain deformation technique is yielded by the Hadamard formulation of HF model and validated at HF level. This approach captures airfoil profile deformation by a modification of the boundary conditions whereas the spatial domain remains unchanged. A mixed POD gathering information from snapshot series associated with several airfoil profiles can be defined. The temporal coefficients in POD expansion are shape-dependent while spatial POD modes are not. In the ROM, airfoil deformation is introduced by a steady forcing term. ROM reliability towards airfoil deformation is demonstrated for the prediction of HF-resolved as well as unknown intermediate configurations.

1. Introduction

The increasing demand concerning the implementation of realistic flow simulations into iterative processes like real-time control, optimal shape design or parametrical studies, highlights the need for hierarchical modeling approaches. In this context, such approaches can provide an interesting balancing between physical accuracy and computational cost. Following this idea, high-fidelity (HF) models characterized by a high physical universality can be replaced by low-dimensional models that represent local approximations of HF models, allowing a strong reduction of the number of degrees of freedom.

The present work focuses on the development of a reduced-order model (ROM) for the prediction of unsteady transonic flows around an airfoil submitted to small deformations. The main contributions of the study are: (i) the elaboration of a ROM of the fully compressible flow non-linear Navier–Stokes equation system by Proper Orthogonal Decomposition (POD)-Galerkin approach, (ii) the introduction of small shape deformations in the ROM on the basis of the Hadamard formulation of HF model and (iii) the analysis of ROM reliability towards small shape deformations.

In the context of model reduction, the technique relying on the Galerkin projection of HF model onto a low-dimensional basis determined by POD, among other approaches, has been widely applied. The POD, also referred to as Principal Component Analysis [1] or Karhunen-Loève expansion [2], was initially utilized in fluid mechanics for coherent structure

* Corresponding author.
E-mail address: bourguet@mit.edu (R. Bourguet).

0021-9991/$ - see front matter © 2010 Elsevier Inc. All rights reserved.
doi:10.1016/j.jcp.2010.09.019

identification in turbulent flows [3]. It is often used to capture main flow features by a low number of basis functions or modes. As a consequence, POD-Galerkin approach is both *physics*- and *data-driven* since HF physical model is present through its Galerkin projection while POD modes are determined from flow snapshot series. The first aspect enforces the physical relevance of the approach while the second is responsible for both dimension reduction and local validity.

On the basis of Navier–Stokes equations and under incompressibility assumption, POD-Galerkin approach has been considered to derive ROMs of laminar and transitional flows predicted by direct numerical simulation [4–10], turbulent flows simulated by large eddy simulation [11] or statistical approaches [12], for example, as well as noisy laminar flows issued from stochastic simulations relying on polynomial chaos representations [13]. Compressible flows have been less investigated, especially in the non-linear fully compressible case. A framework based on POD-Galerkin approach has been reported in [14] for the linearized inviscid Euler equations. Adopting a linearization about a state determined by solving the non-linear governing equations (Euler or viscous-inviscid coupling), ROMs based on time-and frequency-domain POD have been elaborated for the prediction of transonic flows in turbomachinery and airfoil aeroelasticity context [15–18]. An aeroelastic POD ROM of a complete aircraft configuration in the transonic regime has been developed in the frequency domain on the basis of a linearized formulation of HF model [19]. A non-linear extension of frequency-domain POD-based ROM has been developed by means of automatic differentiation [20] and led to efficient prediction of inviscid transonic flows around an airfoil.

The present study concerns non-linear ROM of transonic flows in the time domain. In the fully compressible case, the coupling of the kinematic quantities with two thermodynamic variables induces two main difficulties concerning POD-Galerkin approach. The classical conservative formulation of the state vector does not lead to polynomial fluxes as in the incompressible case. This strongly complexifies the Galerkin projection and does not allow once for all computation of ROM coefficients. Moreover, in this context, the inner product usually considered for POD in the incompressible case is not dimensionally consistent. Under isentropic flow assumption, that is valid for moderate Mach numbers, a ROM of the compressible cavity flow has been put forward [21]. This assumption allows to express the governing equations as quadratic fluxes and an energetic inner product involving both flow and sound velocities can be defined. However, in the fully compressible case, the physical context of this work, the above mentioned difficulties have to be overcome. As reported in the present paper, the two key enablers are a modified state formulation along with constant viscosity assumption that lead to quadratic fluxes [22] and a consistent definition of the non-dimensional inner product as suggested in a preliminary work [23].

Beyond the elaboration of an efficient ROM for unsteady transonic flows, one of the main objectives of this study is to develop a ROM able to handle airfoil small deformations and reliable for the prediction of the effect of such deformations on predominant flow features. From a general point of view, a crucial issue in ROM development is the robustness of its predictive capacities in a certain neighborhood about reference configurations. Within such trust-regions, ROMs are expected to respond similarly to HF model. The integration of POD-Galerkin models into control procedures involving flow actuation [e.g. 24–27] or into parametrical studies concerning Reynolds number for example [4,6,8], has emphasized POD ROM sensitivity. These studies have highlighted inherent issues and limitations of this approach and suggested improvements, especially concerning POD basis validity and the introduction of flow actuation in the ROM. In the present work, these points are addressed in the case of small parametrical deformations of airfoil profile.

In the literature, only a few studies have dealt with ROM of flows around deformed bodies. The approaches based on an actual deformation of the computational grid have to face several issues concerning POD and especially the evaluation of spatial inner products between snapshots associated with different domains [28]. If the number of discretization points is unchanged during deformation, the 'index-based' POD approach [29] can be considered: the discretized POD modes are not associated with a specific spatial location but with space discretization point numbering. A drawback of this approach is the dependency of POD modes on the method considered to propagate the body deformation within the domain. As a consequence, for small deformations, considering a reference domain that is not modified by the deformation and introducing this deformation through a modification of the boundary conditions appears as a convenient alternative. In particular, the 'transpiration' method, that enforces the impermeability condition on the fictitious surface, has been used for both HF modeling [30,31] and ROM [32] on the basis of Euler equations. In the present physical context that concerns viscous flows in the transonic regime, a fictitious domain deformation technique is developed on the basis of the Hadamard formulation of HF model. As discussed in the following, this approach mimics efficiently airfoil deformation at HF level and yields a simple framework for introducing shape deformation in ROM.

The paper is organized as follows. HF model, related numerical method as well as the physical context of the study are briefly described in Section 2. A ROM of the transonic flow past NACA0012 airfoil is elaborated in Section 3 from this HF model via POD-Galerkin approach. In Section 4, a fictitious domain deformation technique is developed and validated at HF level. It is applied in Section 5 where ROM approach is extended to handle airfoil profile deformations. The main findings of the present work are summarized in Section 6.

2. High-fidelity model

The system of the compressible flow Navier–Stokes equations is considered as HF model for the prediction of the present transonic flows. The governing equations are briefly recalled (Section 2.1) as well as the numerical method (Section 2.2). The

physical context of the study that concerns flow unsteadiness induced by compressibility effects is shortly described in Section 2.3.

2.1. Governing equations

The compressible flow is described in Cartesian coordinates. $\cdot_{,t}$ and $\cdot_{,i}$ subscripts denote respectively time and space derivatives. Greek subscripts and superscripts are used for implicit summations. The density is denoted by ρ and the velocity components by u_i. The pressure p satisfies the ideal gas law $p = \rho RT$ where T is the temperature and R is the ideal gas constant ($R = 287$ J kg^{-1} K^{-1} for air). The fluid viscosity μ is evaluated through Sutherland's law:

$$\mu(T) = \mu_0 \sqrt{\frac{T}{T_0}} \frac{1 + \frac{C_s}{T_0}}{1 + \frac{C_s}{T}}, \tag{1}$$

where $C_s = 110.4$ K, $\mu_0 = 1.711 \times 10^{-5}$ Pa s and $T_0 = 273.15$ K. $\tau_{ij} = \mu(u_{i,j} + u_{j,i} - 2/3 u_{\alpha,\alpha}\delta_{ij})$ are the components of the viscous effort tensor where δ_{ij} is Kronecker symbol. The heat flux components q_i are defined as $q_i = -(\gamma_p \mu/\mathrm{Pr}) C_v T_{,i}$, where Pr is Prandtl number, γ_p the polytropic coefficient ($\gamma_p = 1.4$ and Pr = 0.72 are generally considered for air) and $C_v = R/(\gamma_p - 1)$ is the specific heat coefficient. The total energy e is defined as $e = C_v T + u_\alpha^2/2$.

The state vector is denoted by $\boldsymbol{v}$, the inviscid and viscous fluxes of the governing equations by $\boldsymbol{F}_i$ and $\boldsymbol{F}_i^{\mathrm{vis}}$ respectively. The Navier–Stokes equations for unsteady compressible flows can be expressed as follows, in two dimensions:

$$\boldsymbol{v}_{,t} + \boldsymbol{F}_{\alpha,\alpha} = \boldsymbol{F}_{\alpha,\alpha}^{\mathrm{vis}} \quad \text{with} \quad \boldsymbol{v} = \begin{bmatrix} \rho \\ \rho u_1 \\ \rho u_2 \\ \rho e \end{bmatrix}, \quad \boldsymbol{F}_i = \begin{bmatrix} \rho u_i \\ \rho u_i u_1 + p\delta_{1i} \\ \rho u_i u_2 + p\delta_{2i} \\ \rho u_i e + p u_i \end{bmatrix}, \quad \boldsymbol{F}_i^{\mathrm{vis}} = \begin{bmatrix} 0 \\ \tau_{1i} \\ \tau_{2i} \\ \tau_{i\alpha} u_\alpha - q_i \end{bmatrix}. \tag{2}$$

Initial and boundary conditions associated with system (2) are described in the following.

2.2. Two-dimensional Navier–Stokes simulation

Complete description and validation studies of the numerical method have been reported in [33,34] concerning transonic flows around an airfoil at moderate Reynolds numbers. Since a similar transonic flow is considered in this work, only main numerical parameters and computational domain characteristics relevant to the present study are recalled in this section.

2.2.1. Numerical method

The complete time-dependent Navier–Stokes equations are solved in two dimensions under the conservative form (2), in a general non-orthogonal curvilinear coordinate system. A non-dimensional formulation based on chord length (c), uniform upstream velocity and density is considered. The ICARE/IMFT [34] in-house finite volume software for compressible flows around bodies is employed. The Roe upwind scheme [35] with Monotonic Upstream Schemes for Conservative Laws (MUSCL) approach [36] is used for discretization of convection and pressure terms. Diffusion terms are discretized by central differences. Space schemes are second-order accurate. Temporal integration is ensured by an explicit four-stage Runge–Kutta scheme that is second-order accurate [37]. Time step convergence study has been reported in the previously mentioned references.

2.2.2. Computational domain and boundary conditions

The computational domain is presented in Fig. 1. A C-type grid (369×89 points) is used for the present non-confined flow around an airfoil at zero angle of incidence. Especially, $10c$ separate the leading edge from the outflow boundary and $7c$ the trailing edge from the outer boundary. Detailed grid convergence have been previously performed to ensure independance towards both grid refinement and domain size [33,34].

The upstream Mach number $\mathrm{Ma}_\infty = \|\boldsymbol{u}_\infty\|/\sqrt{\gamma_p RT_\infty}$, Reynolds number $\mathrm{Re}_\infty = \rho_\infty \|\boldsymbol{u}_\infty\| c/\mu_\infty$ and flow temperature $T_\infty = 300$ K are imposed as freestream conditions at the outer boundary. Subscript $\cdot_\infty$ denotes upstream quantities. At the outflow boundary a first-order extrapolation of all state variables is used. Along the wake line, the values are specified by averaging the variables from the adjacent points above and below. On the airfoil, the boundary conditions are no-slip and constant temperature. The stagnation temperature is imposed on the airfoil surface:

$$T_{\mathrm{wall}} = \left(1 + \frac{\gamma_p - 1}{2} \mathrm{Ma}_\infty^2\right) T_\infty. \tag{3}$$

An additional condition is used to completely determine the state vector on the airfoil surface. Zero normal density gradient is imposed on the airfoil.

Uniform fields defined from freestream conditions are considered as initial conditions.

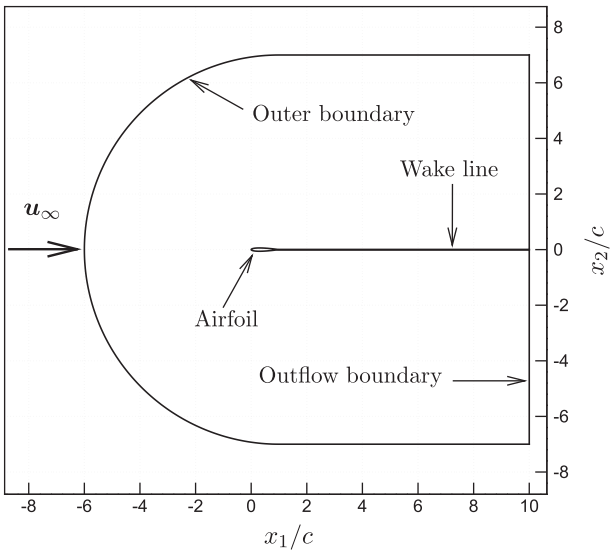

Fig. 1. Sketch of the computational domain. $\boldsymbol{u}_\infty$ denotes upstream velocity.

2.3. Transonic flow past an airfoil at moderate Reynolds numbers

The two-dimensional transonic flow around NACA0012 airfoil at zero angle of incidence and moderate chord-based Reynolds number ($Re_\infty \in [0.5, 1] \times 10^4$) develops an unsteadiness induced by compressibility effects. This flow has been extensively investigated on the basis of numerical simulations [33,34,38]. At incompressible regimes ($Ma_\infty < 0.3$), the flow is steady. As Mach number increases, instability mode and unsteady phenomena emerge leading to transition to turbulence. At $Ma_\infty = 0.3$, an undulation appears in the wake. As Mach number increases, this undulation can trigger the symmetrical recirculation bubbles developing near the trailing edge because of the enlargement of the boundary layers downstream of the acceleration regions. This leads to the onset of the von Kármán instability. In Mach number interval [0.5,0.7], this mode becomes more pronounced and a periodic alternating vortex shedding is clearly developed. At $Ma_\infty = 0.75$, a lower frequency phenomenon related with the oscillation of the supersonic pockets on each side of the airfoil is identified. This unsteadiness is the onset of buffet phenomenon. At higher Reynolds numbers, it is characterized by a strong oscillation of the shock waves [39,40]. Buffet has disappeared at $Ma_\infty = 0.85$ whereas the von Kármán vortex shedding is observed until $Ma_\infty = 0.95$.

In the present study, upstream Mach and Reynolds numbers are 0.85 and 5000 respectively. Flow unsteadiness is thus governed by the von Kármán instability as illustrated in Fig. 2. In Fig. 2(a) and (b), instantaneous iso-contours of Mach number and pressure coefficients $C_p = (p - p_\infty)/(0.5\rho_\infty \|\boldsymbol{u}_\infty\|^2)$ allow to locate the supersonic pockets that are steady in the present case, as well as the vortex street. The alternating shedding pattern is emphasized in Fig. 2(c) by instantaneous iso-contours of non-dimensional vorticity. It is responsible for a periodic oscillation of the aerodynamic lift coefficient, for

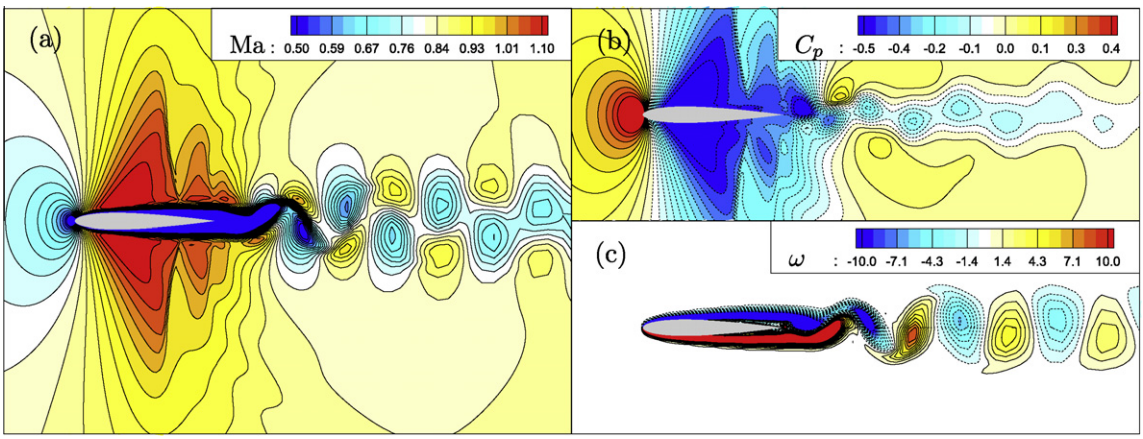

Fig. 2. NACA0012 profile, no incidence, $Ma_\infty = 0.85$, $Re_\infty = 5000$: instantaneous iso-contours of (a) Mach number, (b) pressure coefficient and (c) non-dimensional vorticity. Dashed iso-lines denote negative iso-contours.

example, as illustrated in the following. This transonic flow is considered in the present work to analyze the proposed shape-dependent ROM approach and less regular physical configurations will be envisaged in a future publication. A ROM of this transonic flow around NACA0012 airfoil is elaborated in next section.

3. Reduced-order modeling of transonic flow around NACA0012 airfoil

A ROM of transonic flows is developed by means of Galerkin projection of the compressible flow Navier–Stokes equations onto a low-dimensional basis determined by POD. The issues induced by the coupling of kinematic and thermodynamic variables in the state vector are addressed concerning POD-Galerkin approach in Sections 3.1 and 3.2. A stabilisation procedure for POD-based ROM is presented in Section 3.3. Application to the reference transonic flow around NACA0012 airfoil is provided in Section 3.4 before extending the ROM to handle small shape deformations in next sections.

3.1. Proper Orthogonal Decomposition for compressible flows

The state vector $\boldsymbol{v}$ is decomposed into a mean part $\overline{\boldsymbol{v}}$ and a fluctuating part $\tilde{\boldsymbol{v}}$. The POD is applied to the fluctuating part. It consists in expanding $\tilde{\boldsymbol{v}}$ as a linear combination of specific spatial eigenfunctions $\boldsymbol{\Phi}_i$ weighted by time-dependent coefficients a_i [41]:

$$\boldsymbol{v}(\boldsymbol{x},t) = \overline{\boldsymbol{v}}(\boldsymbol{x}) + \tilde{\boldsymbol{v}}(\boldsymbol{x},t) = \overline{\boldsymbol{v}}(\boldsymbol{x}) + \sum_{i=1}^{\infty} a_i(t)\boldsymbol{\Phi}_i(\boldsymbol{x}) \approx \overline{\boldsymbol{v}}(\boldsymbol{x}) + \sum_{i=1}^{N_{\text{pod}}} a_i(t)\boldsymbol{\Phi}_i(\boldsymbol{x}), \tag{4}$$

where N_{pod} is the number of retained POD modes. Since the POD is applied to the fluctuating part, the steady boundary conditions of HF model that linearly depend on the state vector are satisfied exactly by any truncated POD expansion (4). In the following, $\langle\cdot\rangle$ denotes the time-averaging operator and $(\cdot,\cdot)_\Omega$ a spatial inner product that has to be defined on the domain $\Omega \subset \mathbb{R}^2$. An energy-based inner product has been reported in [21] for isentropic flows. In the fully compressible case considered in the present study, the kinematic variables are associated with two thermodynamic quantities. The number of state variables is denoted by d ($d = 4$ in the two-dimensional case). A dimensionally consistent inner product can be reached by a normalization of each state variable contribution by the corresponding space-averaged variance σ_i^2 as follows, for two given states, $\boldsymbol{v}^I$ and $\boldsymbol{v}^{II}$:

$$\left(\boldsymbol{v}^I, \boldsymbol{v}^{II}\right)_\Omega = \sum_{i=1}^{d} \frac{1}{\sigma_i^2} \int_\Omega v_i^I v_i^{II} d\boldsymbol{x} \quad \text{with} \quad \sigma_i^2 = \int_\Omega \langle \tilde{v}_i^2 \rangle d\boldsymbol{x}. \tag{5}$$

This inner product involves a systematic normalization procedure previously used in [42]. This approach avoids dependency on a given non-dimensional formulation of the governing equations. The orthogonal projector onto span$\{\boldsymbol{\Phi}_1,\ldots,\boldsymbol{\Phi}_i\}$ for $i \geqslant 1$, is denoted by Π_i with $\Pi_0 \equiv \boldsymbol{0}$. The orthonormal spatial POD modes are the successive solutions of the following optimization problem:

$$\boldsymbol{\Phi}_{i+1} = \arg\max_{\boldsymbol{\Psi}} \langle (\tilde{\boldsymbol{v}} - \Pi_i \tilde{\boldsymbol{v}}, \boldsymbol{\Psi})_\Omega^2 \rangle \quad \text{with} \quad (\boldsymbol{\Psi},\boldsymbol{\Psi})_\Omega = 1. \tag{6}$$

Following 'snapshot-POD' approach [43], solving the optimization problem (6) is equivalent to solve the following eigenproblem involving the two-point time correlation tensor $K(t,t') = (\tilde{\boldsymbol{v}}(\cdot,t), \tilde{\boldsymbol{v}}(\cdot,t'))_\Omega$:

$$\langle K(t,\cdot)\psi_i \rangle_{(t')} = \lambda_i \psi_i(t) \quad \text{with} \quad \langle \psi_i \psi_j \rangle = \delta_{ij}. \tag{7}$$

Subscript $\cdot_{(t')}$ indicates that the integration involves the second time variable of K while t is fixed. The spatial POD modes that convey statistical content can be evaluated from the eigenfunctions ψ_i associated with positive eigenvalues λ_i ($\lambda_1 \geqslant \lambda_2 \geqslant \cdots > 0$) as follows:

$$\boldsymbol{\Phi}_i(\boldsymbol{x}) = \frac{1}{\sqrt{\lambda_i}} \langle \tilde{\boldsymbol{v}}(\boldsymbol{x},\cdot)\psi_i \rangle. \tag{8}$$

In the discrete context, 'snapshot-POD' approach is generally considered when the number of space discretization point (N_x) is higher than the number of flow samples or snapshots in time series (N_t). This is the case in the present work where snapshots are issued from numerical simulation. Moreover N_{pod} is expected to be small as compared to N_x and N_t.

3.2. POD-Galerkin model

The compressible flow Navier–Stokes equations are expressed as quadratic fluxes by means of the following variable change [22] and assuming constant viscosity μ:

$$\boldsymbol{v} = \begin{bmatrix} \rho \\ \rho u_1 \\ \rho u_2 \\ \rho e \end{bmatrix} \rightarrow \boldsymbol{w} = \begin{bmatrix} 1/\rho \\ u_1 \\ u_2 \\ p \end{bmatrix}. \tag{9}$$

Considering variable change (9), HF governing Eq. (2) can be written as follows:

$$\boldsymbol{w}_{,t} + \boldsymbol{G}_\alpha \boldsymbol{w}_{,\alpha} = \boldsymbol{G}_\alpha^{\text{vis}} \quad \text{with} \tag{10}$$

$$\boldsymbol{G}_i = \begin{bmatrix} u_i & -(1/\rho)\delta_{1i} & -(1/\rho)\delta_{2i} & 0 \\ 0 & u_i & 0 & (1/\rho)\delta_{1i} \\ 0 & 0 & u_i & (1/\rho)\delta_{2i} \\ 0 & \gamma_p p\delta_{1i} & \gamma_p p\delta_{2i} & u_i \end{bmatrix} \quad \text{and} \quad \boldsymbol{G}_i^{\text{vis}} = \begin{bmatrix} 0 \\ (1/\rho)\tau_{1i,i} \\ (1/\rho)\tau_{2i,i} \\ \frac{\gamma_p \mu}{\text{Pr}}(p/\rho)_{,ii} + \left(\gamma_p - 1\right) u_{\alpha,i}\tau_{\alpha i} \end{bmatrix}. \tag{11}$$

The ith POD mode associated with state vector $\boldsymbol{w}$ is expressed as follows:

$$\boldsymbol{\Phi}_i = \begin{bmatrix} \Phi_i^{(1/\rho)} \\ \Phi_i^{u_1} \\ \Phi_i^{u_2} \\ \Phi_i^{p} \end{bmatrix}. \tag{12}$$

The Galerkin projection of (10) onto the N_{pod}-dimensional POD basis yields the following quadratic polynomial ODE system, under constant viscosity assumption, for $i = 1,\ldots,N_{\text{pod}}$:

$$\begin{cases} \dot{a}_i = \left(C_i + C_i^{\text{c}}\right) + \sum\limits_{j=1}^{N_{\text{pod}}} \left(L_{ij} + L_{ij}^{\text{c}}\right) a_j + \sum\limits_{j,k=1}^{N_{\text{pod}}} Q_{ijk} a_j a_k = f_i\left(\boldsymbol{C}^{\text{c}}, \boldsymbol{L}^{\text{c}}, \boldsymbol{a}\right), \\ a_i(0) = (\boldsymbol{w}(\cdot,0) - \overline{\boldsymbol{w}}, \boldsymbol{\Phi}_i)_\Omega. \end{cases} \tag{13}$$

C_i, L_{ij} and Q_{ijk} are 'physics-driven' coefficients issued from the Galerkin projection while C_i^{c} and L_{ij}^{c} are additional calibration coefficients included to ensure ROM accuracy as detailed in Section 3.3. The constant coefficients issued from the Galerkin projection are computed as follows:

$$C_i = (\boldsymbol{G}_{11}^{\text{vis},\alpha} - \boldsymbol{G}_1^\alpha \check{\boldsymbol{\Phi}}_{1,\alpha}, \boldsymbol{\Phi}_i)_\Omega, \tag{14a}$$

$$L_{ij} = (\boldsymbol{G}_{1(j+1)}^{\text{vis},\alpha} + \boldsymbol{G}_{(j+1)1}^{\text{vis},\alpha} - \boldsymbol{G}_1^\alpha \check{\boldsymbol{\Phi}}_{j+1,\alpha} - \boldsymbol{G}_{j+1}^\alpha \check{\boldsymbol{\Phi}}_{1,\alpha}, \boldsymbol{\Phi}_i)_\Omega, \tag{14b}$$

$$Q_{ijk} = (\boldsymbol{G}_{(j+1)(k+1)}^{\text{vis},\alpha} - \boldsymbol{G}_{j+1}^\alpha \check{\boldsymbol{\Phi}}_{k+1,\alpha}, \boldsymbol{\Phi}_i)_\Omega, \tag{14c}$$

where $\check{\boldsymbol{\Phi}} = [\overline{\boldsymbol{w}}\boldsymbol{\Phi}_1 \cdots \boldsymbol{\Phi}_{N_{\text{pod}}}]$. $\boldsymbol{G}_j^i$ and $\boldsymbol{G}_{jk}^{\text{vis},i}$ terms involved in the implicit summations in (14a)–(14c) are defined as follows:

$$\boldsymbol{G}_j^i = \begin{bmatrix} \check{\Phi}_j^{u_i} & -\check{\Phi}_j^{(1/\rho)}\delta_{1i} & -\check{\Phi}_j^{(1/\rho)}\delta_{2i} & 0 \\ 0 & \check{\Phi}_j^{u_i} & 0 & \check{\Phi}_j^{(1/\rho)}\delta_{1i} \\ 0 & 0 & \check{\Phi}_j^{u_i} & \check{\Phi}_j^{(1/\rho)}\delta_{2i} \\ 0 & \gamma_p\check{\Phi}_j^{p}\delta_{1i} & \gamma_p\check{\Phi}_j^{p}\delta_{2i} & \check{\Phi}_j^{u_i} \end{bmatrix} \quad \text{and} \quad \boldsymbol{G}_{jk}^{\text{vis},i} = \begin{bmatrix} 0 \\ \check{\Phi}_j^{(1/\rho)}\check{\tau}_{1ik,i} \\ \check{\Phi}_j^{(1/\rho)}\check{\tau}_{2ik,i} \\ \frac{\gamma_p\mu}{\text{Pr}}\left(\check{\Phi}_j^{p}\check{\Phi}_k^{(1/\rho)}\right)_{,ii} + (\gamma_p - 1)\check{\Phi}_{j,i}^{u_\alpha}\check{\tau}_{\alpha ik} \end{bmatrix}, \tag{15}$$

where $\check{\tau}_{ijk} = \mu(\check{\Phi}_{k,j}^{u_i} + \check{\Phi}_{k,i}^{u_j} - 2/3\check{\Phi}_{k,\alpha}^{u_\alpha}\delta_{ij})$. For given POD basis and mean flow, ROM coefficients can be computed a priori and once for all. The evaluation of the additional coefficients C_i^{c} and L_{ij}^{c} involved in ROM (13) is described in next section.

HF model boundary conditions appear in the ROM through POD basis functions. As previously mentioned, steady conditions depending linearly on the state vector are exactly satisfied while other ones are approximated through expansion (4).

3.3. Calibration procedure

As reported in [7,11] for example, dynamical systems issued from POD-Galerkin approach can suffer from an unstable character that can lead to erroneous predictions. In laminar regime, this lack of accuracy can be induced both by the assumptions made during ROM elaboration, as for example considering a constant viscosity in the present case, and by POD basis truncation that can modify the dynamical system stability properties. The latest point has been emphasized on model problems in [7,44] and is referred to as ROM structural instability. In a similar way, in turbulent regime, the fact that some dissipative structures, that play a major role in flow energy balance, are neglected when POD basis is truncated, can be a source of error in the ROM. Many approaches have been suggested to enforce ROM accuracy, among others: addition of artificial viscosity [45,46], calibration procedures [8,10,11], addition of penalization terms [5,22], introduction of shift modes [7], Navier–Stokes residual-based procedures [47].

A calibration method is adopted here in a similar way to [11] in the incompressible case. This approach consists in minimizing ROM prediction error with respect to reference dynamics issued from the projection of HF snapshots onto POD basis:

$$a_i^{\text{pod}} = (\tilde{\boldsymbol{w}}, \boldsymbol{\Phi}_i)_\Omega, \tag{16}$$

while controlling calibration cost. The following prediction error is considered:

$$E(\boldsymbol{C}^c, \boldsymbol{L}^c) = \sum_{i=1}^{N_{pod}} \int_0^{T_s} \left(a_i^{pod} - a_i^{pod}(0) - \int_0^t f_i(\boldsymbol{C}^c, \boldsymbol{L}^c, \boldsymbol{a}^{pod}) dt' \right)^2 dt, \tag{17}$$

where T_s is the time interval of snapshot series and f_i is the right-hand side of ROM (13). Reference temporal coefficients a_i^{pod} (16) are used in the Cauchy problem integration instead of those issued from ROM (13) integration. This linearizes the optimization problem solved during calibration procedure as detailed at the end of this section. Other definitions could be envisaged for ROM prediction error as the error between reference dynamic derivatives and f_i, for example. The following normalized error is considered in calibration procedure:

$$\mathcal{E}(\boldsymbol{C}^c, \boldsymbol{L}^c) = \frac{E(\boldsymbol{C}^c, \boldsymbol{L}^c)}{E(\boldsymbol{0}_{N_{pod}}, \boldsymbol{0}_{N_{pod}^2})}. \tag{18}$$

The calibration cost measures the weight of the calibration coefficients compared to those issued from Galerkin projection (C_i and L_{ij} in (13)):

$$\mathcal{C}(\boldsymbol{C}^c, \boldsymbol{L}^c) = \frac{\|\boldsymbol{C}^c\|_{N_{pod}}^2 + \|\boldsymbol{L}^c\|_{N_{pod}^2}^2}{\|\boldsymbol{C}\|_{N_{pod}}^2 + \|\boldsymbol{L}\|_{N_{pod}^2}^2}, \tag{19}$$

where the norms are defined by $\|\boldsymbol{C}\|_{N_{pod}}^2 = C_\alpha^2$ and $\|\boldsymbol{L}\|_{N_{pod}^2}^2 = L_{\alpha\beta}^2$.

The calibration coefficients C_i^c and L_{ij}^c in (13) are found by minimizing the following function that balances ROM prediction error and calibration cost by means of a blending coefficient $0 < \theta < 1$:

$$\mathcal{J}(\boldsymbol{C}^c, \boldsymbol{L}^c, \theta) = \theta \mathcal{E}(\boldsymbol{C}^c, \boldsymbol{L}^c) + (1-\theta)\mathcal{C}(\boldsymbol{C}^c, \boldsymbol{L}^c). \tag{20}$$

The blending coefficient θ can also be regarded as a regularization parameter in Tikhonov regularization framework [48,49].

Gathering all calibration coefficients in a single matrix $\boldsymbol{K}^c = [\boldsymbol{C}^c \boldsymbol{L}^c]$, minimizing $\mathcal{J}$ is equivalent to solve the following N_{pod} linear systems of size $N_{pod} + 1$:

$$\boldsymbol{A}^c (\boldsymbol{K}_{i\cdot}^c)^t = \boldsymbol{b}^i, \tag{21}$$

where superscript $\cdot^t$ denotes the transposition and $\boldsymbol{K}_{i\cdot}^c$ the ith row of $\boldsymbol{K}^c$. $\boldsymbol{A}^c$ and $\boldsymbol{b}^i$ are defined as follows:

$$A_{ij}^c = \int_0^{T_s} \left(\int_0^t \breve{a}_i dt' \right) \left(\int_0^t \breve{a}_j dt' \right) dt + \tilde{\theta}\delta_{ij} \tag{22}$$

and

$$b_i^j = \int_0^{T_s} \left(a_j^{pod} - a_j^{pod}(0) - \int_0^t f_j\left(\boldsymbol{0}_{N_{pod}}, \boldsymbol{0}_{N_{pod}^2}, \boldsymbol{a}^{pod}\right) dt' \right) \left(\int_0^t \breve{a}_i dt' \right) dt, \tag{23}$$

with

$$\tilde{\theta} = \frac{(1-\theta)}{\theta} \frac{E\left(\boldsymbol{0}_{N_{pod}}, \boldsymbol{0}_{N_{pod}^2}\right)}{\|\boldsymbol{C}\|_{N_{pod}}^2 + \|\boldsymbol{L}\|_{N_{pod}^2}^2} \quad \text{and} \quad \breve{\boldsymbol{a}} = [1 \; a_1^{pod} \cdots a_{N_{pod}}^{pod}]. \tag{24}$$

3.4. Application: transonic flow past NACA0012 airfoil

The previous low-dimensional modeling approach is applied to build a ROM of the transonic flow past NACA0012 airfoil at zero angle of incidence, at the above mentioned Mach and Reynolds numbers. POD basis is extracted from $N_t = 100$ snapshots collected over one period of the von Kármán vortex shedding of Strouhal number $St = f^{vk}c/\|\boldsymbol{u}_\infty\| = 1.340$. f^{vk} is the dimensional fundamental frequency of the vortex shedding. This number of flow samples or lower ones are generally considered for laminar flows with a strong periodic character [e.g. 4,8] but similar results have been reached in the present case with $N_t = 30$, for example. The statistical content of each POD mode is measured by the relative magnitude of the corresponding eigenvalue (λ_i) of time correlation tensor K (7). This is shown in Fig. 3, as well as the cumulative statistical content conveyed by the truncated basis, defined by:

$$I_{N_{pod}} = \frac{\sum_{i=1}^{N_{pod}} \langle (\tilde{\boldsymbol{w}}, \boldsymbol{\Phi}_i)_\Omega^2 \rangle}{\langle \|\tilde{\boldsymbol{w}}\|_\Omega^2 \rangle}, \tag{25}$$

where $\|\cdot\|_\Omega$ is the norm induced by inner product (5). If the projected dataset in (25) is the same as the one used to extract POD modes then $I_{N_{pod}} = \sum_{i=1}^{N_{pod}} \lambda_i / \sum_{i=1}^{N_t} \lambda_i$. Here, $N_{pod} = 10$ modes are retained which allows to capture more than 99.99% of snapshot series statistical content.

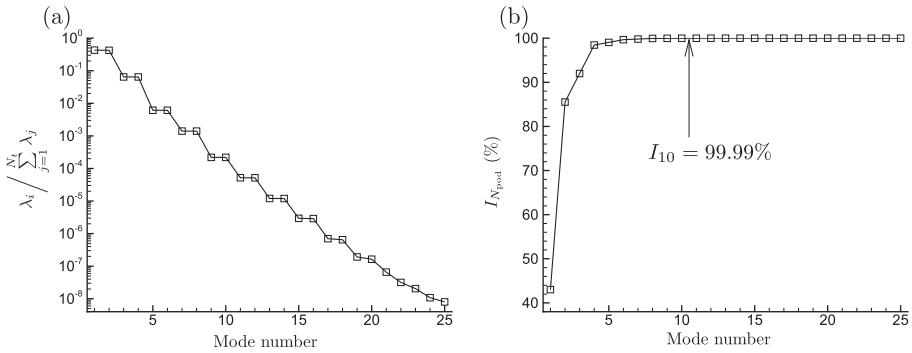

Fig. 3. (a) Relative statistical content of each POD mode and (b) relative statistical content of the truncated POD basis as a function of mode number.

In Fig. 4 selected POD modes associated with u_1 and p are qualitatively presented. These modes do not represent flow structures but can provide information about space correlations for example [23,50]. Their symmetric/antisymmetric patterns about the wake line have been previously reported for incompressible periodic flows governed by the von Kármán instability [e.g. [4,7].

Reference temporal evolutions of these modes, a_i^{pod} (16), are shown in Fig. 5 (circles). A ROM is built from the mean flow and the 10-dimensional POD basis. It is integrated over one vortex shedding period from the exact initial condition $\boldsymbol{a}^{\text{pod}}(0)$. ROM integration is ensured by a fourth-order-accurate four-stage Runge–Kutta scheme.

While the first temporal coefficients are qualitatively well predicted, amplitude and phase drifts are observed for higher index modes (Fig. 5(a)–(c), plain lines). This illustrates the previously mentioned unstable behavior of POD ROMs. The calibration diagram showing the absolute prediction error E (17) as a function of the calibration cost $\mathcal{C}$ (19) is plotted in Fig. 6 (plain line). In addition, the effective error evaluated afterwards in a similar way to E but involving the predicted coefficients a_i^{rom} in the Cauchy problem integration (17) instead of reference ones is also plotted (dashed line). As functions of $\mathcal{C}$, both prediction errors exhibit similar behaviors. A calibration cost $\mathcal{C} = 20\%$ is considered. This leads to stable and accurate predictions (Fig. 5(d)–(f)). This calibration cost threshold is retained in the following. It is shown in Section 5.3 that, despite calibration procedure, the ROM remains sensitive to changes in the physical configuration and especially to airfoil profile deformation.

The present application exemplifies POD ROM approach from a qualitative point of view. In the following, airfoil shape deformation is introduced and quantitative error analysis is provided in this context.

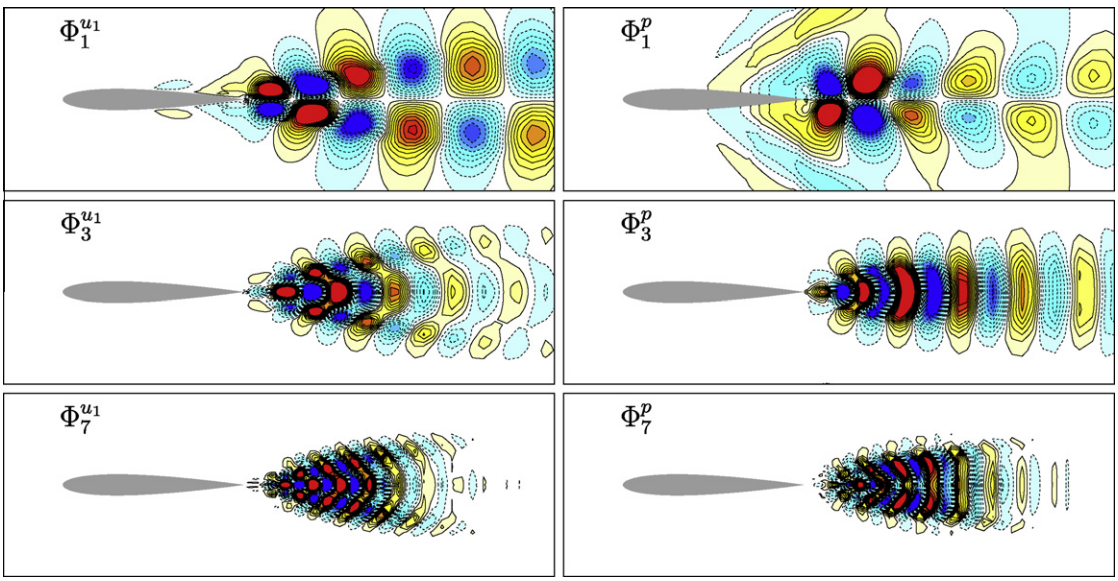

Fig. 4. 1st, 3rd and 7th POD modes associated with longitudinal velocity (left) and pressure (right). Plain/dashed iso-lines denote positive/negative valued iso-contours.

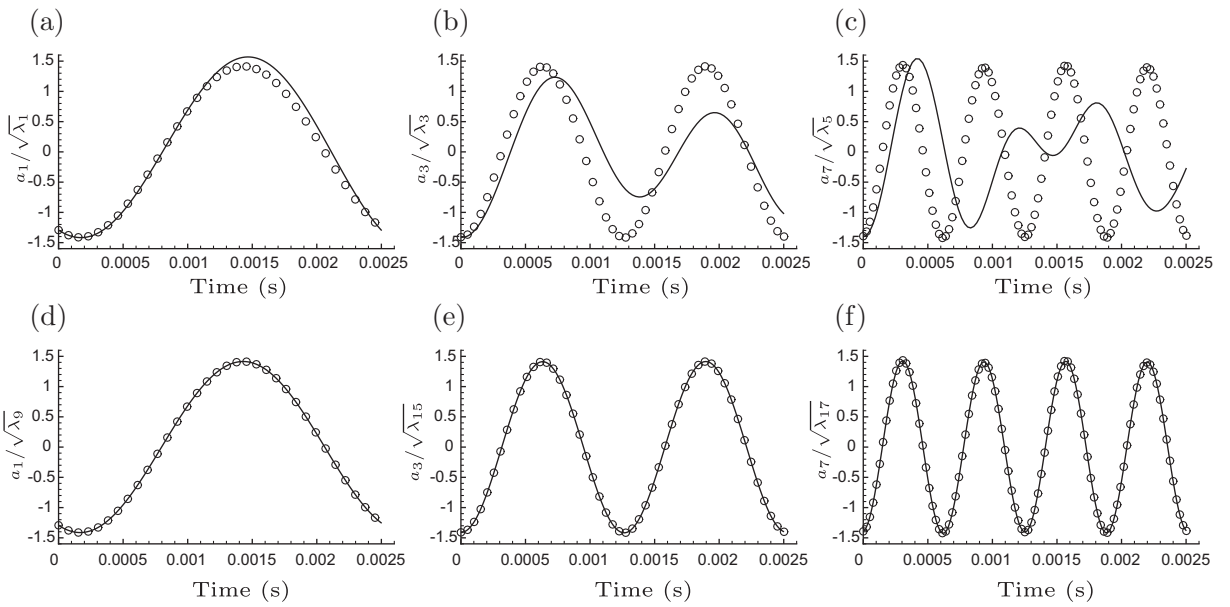

Fig. 5. Time-history of selected POD coefficients issued from: snapshot projection onto POD modes (a_i^{pod}, circles), ROM integration (a_i^{rom}, plain lines), over one period of the von Kármán vortex shedding: (a)–(c) uncalibrated and (d)–(f) calibrated ROMs.

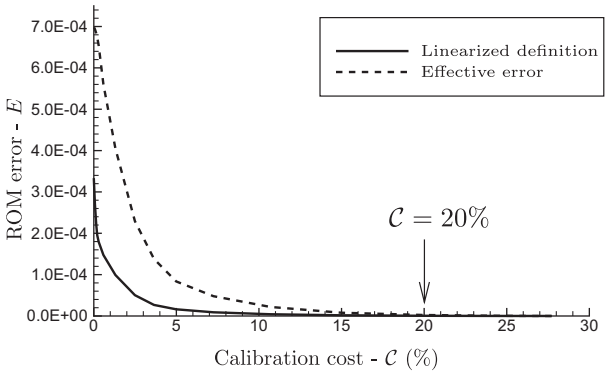

Fig. 6. Prediction error as functions of calibration cost. The arrow indicates the retained calibration cost.

4. Airfoil deformation

Different approaches can be envisaged to take into account of airfoil profile deformation in the ROM. However, defining rigorously a POD basis valid for distinct spatial domains associated to several airfoil profiles presents some difficulties. Two main issues arise: the practical issue of dealing with different domains concerning the spatial inner product and the actual deformation of POD modes, and the validity of POD basis over a certain range of deformations. The latest point, that is an inherent difficulty concerning the use of POD ROM for parametrical studies, is addressed in Section 5.1. The present section focuses on the first point. Considering a single POD basis on different domains implies an appropriate mapping of POD modes to each deformed configuration. This point was solved in [29] by means of an 'index-based' POD where the discretized modes are not associated with a specific spatial location but with space discretization point numbering. This approach allows to handle snapshots issued from distinct deformed domains. Nonetheless, this implies that POD modes directly depend on the technique utilized to deform the grid and thus the amount of statistical content conveyed by the low-dimensional basis also depends on this procedure. An extension of this technique was also developed by considering several POD bases [51]. From a general point of view, a specific POD basis could be considered for each deformed configuration. As shown in [52] for example, POD basis interpolation methods exist for parametrical studies. However, when the parametrical study involves spatial domain modification, the application of this type of procedures is not trivial. Moreover, the evaluation of a specific POD basis for each new profile implies a new computation of all ROM coefficients, which can be numerically expensive, especially if N_x is large.

Therefore, an alternative can consist in considering a reference spatial domain that is not altered by shape deformations. On such a domain, airfoil profile modification could be introduced through an additional forcing term in the governing equations, following immersed boundary method [53], for example. A new methodology, originally inspired by 'transpiration' approach for Euler equations [31] and that does not require modification of the governing equations is suggested in the present study, for small shape deformations. This approach relies on the Hadamard formulation [54] of HF model which was previously used in the context of optimal shape design on the basis of Euler equations [55,56].

As detailed in the following, this technique yields fictitious boundary conditions that allow to mimic airfoil deformation on a reference domain with no modification of HF governing equations. This can be used to derive simple ROM able to predict airfoil deformation effects on flow evolution, as reported in next section.

In this section, the fictitious deformation approach on a fixed reference domain is described (Section 4.1) and validated on HF model (Section 4.2).

4.1. Hadamard formulation for domain deformation

In his pioneering work [57], Hadamard studied the variation of the solution of a partial differential equation with respect to its domain Ω_γ in the neighborhood of a reference domain Ω_0. He demonstrated that this variation can be well defined on the reference domain. This Hadamard derivative is the solution of a differentiated partial differential equation with a boundary source term distributed on $\Gamma_0 = \partial\Omega_0$ which is linear with respect to the boundary variation. Following Hadamard, the boundary variation is parameterized by a normal displacement $\gamma\boldsymbol{n}$ (Fig. 7):

$$\Gamma_\gamma = \{\boldsymbol{x} = \boldsymbol{x}_0 + \gamma(\boldsymbol{x}_0)\boldsymbol{n}(\boldsymbol{x}_0),\ \forall \boldsymbol{x}_0 \in \Gamma_0\}. \tag{26}$$

In the following, $\boldsymbol{R}$ denotes the differential volumic residual:

$$\boldsymbol{R}(\boldsymbol{v}) = \boldsymbol{v}_{,t} + \boldsymbol{F}_{\alpha,\alpha} - \boldsymbol{F}^{\text{vis}}_{\alpha,\alpha}, \tag{27}$$

using the same notations as in (2). $\boldsymbol{C}$ holds for boundary residuals. The boundary residuals involve residuals at all boundaries. Only the residual on the airfoil surface needs to be specified here:

$$\boldsymbol{C}(\boldsymbol{v}) = \begin{bmatrix} \nabla_{\boldsymbol{n}}\rho \\ u_1 \\ u_2 \\ T - T_{\text{wall}} \end{bmatrix}, \tag{28}$$

where $\nabla_{\boldsymbol{n}}$ is the profile outward normal gradient.

For a given geometry Ω_γ defined by γ, $\boldsymbol{v}^{\text{NS}}(\gamma)$ is the set of flow variables solving the HF Navier–Stokes equations as introduced in (2). In an integral formulation where $\boldsymbol{\Psi}_1$, $\boldsymbol{\Psi}_2$ and * correspond respectively to two test functions and to a dimensionally consistent scalar product in $\mathbb{R}^4$, this can be written as follows:

$$\boldsymbol{v}^{\text{NS}} = \begin{bmatrix} \rho^{\text{NS}} \\ \rho^{\text{NS}} u_1^{\text{NS}} \\ \rho^{\text{NS}} u_2^{\text{NS}} \\ \rho^{\text{NS}} e^{\text{NS}} \end{bmatrix}, \tag{29}$$

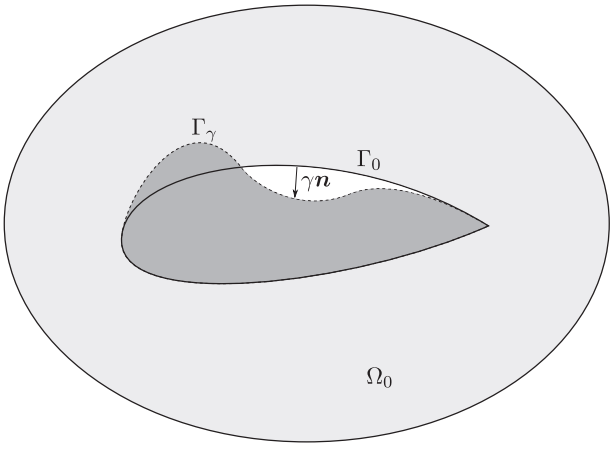

Fig. 7. Reference domain and modified boundary.

$$\boldsymbol{v} = \boldsymbol{v}^{\mathrm{NS}}(\gamma) \Longleftrightarrow \int_{\Omega_\gamma} \boldsymbol{\Psi}_1 * \boldsymbol{R}(\boldsymbol{v}) d\boldsymbol{x} + \int_{\Gamma_\gamma} \boldsymbol{\Psi}_2 * \boldsymbol{C}(\boldsymbol{v}) d\sigma = 0, \ \forall \boldsymbol{\Psi}_1, \boldsymbol{\Psi}_2. \tag{30}$$

(30) defines $\boldsymbol{v}^{\mathrm{NS}}(\gamma)$ as soon as γ is given. The delicate point is that $\boldsymbol{v}^{\mathrm{NS}}(\gamma)$ is defined on a domain Ω_γ which varies with γ. The contribution of Hadamard and of other workers addressing this issue is to give a rigorous context to the differentiation of $\boldsymbol{v}^{\mathrm{NS}}(\gamma)$ with respect to γ. The reader interested in this theory can examine Refs. [54,57,58]. In the following, this method is applied to (30).

For a variation $\delta\gamma$ of the shape, the variation $\delta\boldsymbol{v}^{\mathrm{NS}}$ of the flow unknown $\boldsymbol{v}^{\mathrm{NS}}$ is approximated by the following truncated Taylor formula that is second-order accurate with respect to an adhoc norm of $\delta\gamma$:

$$\delta\boldsymbol{v}^{\mathrm{NS}}(\gamma, \delta\gamma) = \boldsymbol{v}^{\mathrm{NS}}(\gamma + \delta\gamma) - \boldsymbol{v}^{\mathrm{NS}}(\gamma) \approx \frac{\partial \boldsymbol{v}^{\mathrm{NS}}}{\partial \gamma}(\gamma)\delta\gamma. \tag{31}$$

RHS in (31) is obtained from the total derivative of the flow Eq. (30):

$$\begin{aligned} &\int_{\Omega_\gamma} \boldsymbol{\Psi}_1 * \frac{\partial \boldsymbol{R}}{\partial \boldsymbol{v}} \frac{\partial \boldsymbol{v}}{\partial \gamma} \delta\gamma d\boldsymbol{x} + \int_{\Gamma_\gamma} \boldsymbol{\Psi}_2 * \frac{\partial \boldsymbol{C}}{\partial \boldsymbol{v}} \frac{\partial \boldsymbol{v}}{\partial \gamma} \delta\gamma d\sigma + \int_{\Gamma_\gamma} \boldsymbol{\Psi}_1 * \boldsymbol{R}(\boldsymbol{v}) \delta\gamma d\sigma \\ &\quad + \int_{\Gamma_\gamma} \boldsymbol{\Psi}_2 * \nabla_{\boldsymbol{n}} \boldsymbol{C}(\boldsymbol{v}) \delta\gamma d\sigma + \int_{\Gamma_\gamma} \boldsymbol{\Psi}_2 * \mathcal{H}\boldsymbol{C}(\boldsymbol{v}) \delta\gamma d\sigma = 0, \quad \forall \boldsymbol{\Psi}_1, \boldsymbol{\Psi}_2, \end{aligned} \tag{32}$$

where $\mathcal{H}$ is Γ_γ curvature. Since $\boldsymbol{v}^{\mathrm{NS}}(\gamma)$ is solution of the flow system for γ, then the third and fifth integrals in (32) vanish.

In the following, a small perturbation $\delta\gamma$ is considered about $\gamma = 0$:

$$\boldsymbol{v}^{\mathrm{NS}}(\delta\gamma) = \boldsymbol{v}^{\mathrm{NS}}(0) + \delta\boldsymbol{v}^{\mathrm{NS}}(0, \delta\gamma) \tag{33}$$

$$\text{and} \quad \delta\boldsymbol{v}^{\mathrm{NS}}(0, \delta\gamma) \approx \frac{\partial \boldsymbol{v}^{\mathrm{NS}}}{\partial \gamma}(0)\delta\gamma. \tag{34}$$

The differential volumic term can be approximated as follows, without loosing second order accuracy:

$$\begin{aligned} \boldsymbol{R}\big(\boldsymbol{v}^{\mathrm{NS}}(\delta\gamma)\big) &\approx \boldsymbol{R}\big(\boldsymbol{v}^{\mathrm{NS}}(0)\big) + \frac{\partial \boldsymbol{R}}{\partial \boldsymbol{v}}\big(\boldsymbol{v}^{\mathrm{NS}}(0)\big)\delta\boldsymbol{v}^{\mathrm{NS}}(0, \delta\gamma) \\ &\approx \boldsymbol{R}\big(\boldsymbol{v}^{\mathrm{NS}}(0)\big) + \frac{\partial \boldsymbol{R}}{\partial \boldsymbol{v}}\big(\boldsymbol{v}^{\mathrm{NS}}(0)\big)\frac{\partial \boldsymbol{v}^{\mathrm{NS}}}{\partial \gamma}(0)\delta\gamma. \end{aligned} \tag{35}$$

A similar approximation can be considered for $\boldsymbol{C}(\boldsymbol{v}^{\mathrm{NS}}(\delta\gamma))$.

Then, summing (30) and (32) for $\gamma = 0$ yields:

$$\int_{\Omega_0} \boldsymbol{\Psi}_1 * \boldsymbol{R}\big(\boldsymbol{v}^{\mathrm{NS}}(\delta\gamma)\big) d\boldsymbol{x} + \int_{\Gamma_0} \boldsymbol{\Psi}_2 * \boldsymbol{C}\big(\boldsymbol{v}^{\mathrm{NS}}(\delta\gamma)\big) d\sigma \approx -\int_{\Gamma_0} \boldsymbol{\Psi}_2 * \nabla_{\boldsymbol{n}} \boldsymbol{C}\big(\boldsymbol{v}^{\mathrm{NS}}(0)\big)\delta\gamma d\sigma, \quad \forall \boldsymbol{\Psi}_1, \boldsymbol{\Psi}_2. \tag{36}$$

Neglecting smaller terms, (36) is used as the equation defining an approximation of $\boldsymbol{v}^{\mathrm{NS}}(\delta\gamma)$ that is denoted by $\boldsymbol{v}^{\mathrm{H}}(\delta\gamma)$ in the following. As a consequence, the flow solution associated with deformed domain $\Omega_{\delta\gamma}$ is approximated by the solution of Navier–Stokes equations on reference domain Ω_0 with an extra boundary source term. In contrast to the usual Hadamard formulation, the non-linear expression of HF model is retained in the left hand side of (36).

Formulation (36) produces an unsteady right-hand side on the boundary even if shape perturbation $\delta\gamma$ is steady. Indeed, reference flow ($\delta\gamma = 0$) does fluctuate with time. As a first step in the present study the time variation of the normal gradients is neglected. This is justified here by the quasi-steady character of these quantities in the near-wall region of interest. They are frozen at the mean values, denoted as previously by an overline. The Hadamard formulation thus yields the following boundary conditions on the airfoil surface in reference geometry (Ω_0):

$$\begin{aligned} &\nabla_{\boldsymbol{n}} \rho^{\mathrm{H}}(\delta\gamma)(\boldsymbol{x}, t) = -\nabla_{\boldsymbol{n}} \nabla_{\boldsymbol{n}} \overline{\rho^{\mathrm{NS}}}(0)(\boldsymbol{x})\delta\gamma(\boldsymbol{x}), \\ &u_i^{\mathrm{H}}(\delta\gamma)(\boldsymbol{x}, t) = -\nabla_{\boldsymbol{n}} \overline{u_i^{\mathrm{NS}}}(0)(\boldsymbol{x})\delta\gamma(\boldsymbol{x}) \quad \text{for } i = 1, 2, \\ &T^{\mathrm{H}}(\delta\gamma)(\boldsymbol{x}, t) = T_{\mathrm{wall}} - \nabla_n \overline{T^{\mathrm{NS}}}(0)(\boldsymbol{x})\delta\gamma(\boldsymbol{x}). \end{aligned} \tag{37}$$

The impact of the different approximations made in this analysis needs to be evaluated. This is done in next section.

4.2. Validation at HF level

The objective of this validation study is to quantify the agreement between HF simulations performed on deformed grids (referred to as NS) and on the reference NACA0012 grid with fictitious boundary conditions (37) issued from the Hadamard formulation of HF model (referred to as H), taking into account that the suggested approach does not involve any modification of the governing equations. The following deformation, that depends on the shape parameter κ, is applied along the outward normal vector, to the discretized profile:

$$\delta\gamma(\kappa)(\boldsymbol{x}^i) = \kappa \times 0.006\left(\exp\left(-\frac{(i-67)^2}{50}\right) + \exp\left(-\frac{(i-117)^2}{50}\right)\right) \quad \text{for } i \in \{1,\ldots,183\}, \tag{38}$$

where points $\boldsymbol{x}^i$ are located at the trailing edge for $i = 0/184$, at the leading edge for $i = 92$ and at $x_1/c = 0.306$, at the lower/upper side of the airfoil, for $i = 67/117$. The shape parameter κ defines the symmetrical perturbation amplitude. Two deformed profiles are considered in this section: $\kappa = \{-1, 1\}$, which corresponds in each case to 10% variation of airfoil thickness, as illustrated in Fig. 8. $\kappa = 0$ leads to NACA0012 profile.

Mean flows issued from NS and H simulations are compared in Fig. 9. For each state variable in modified formulation (9), $\kappa = -1$ ($\kappa = 1$) field is shown in the upper part (lower part respectively) of Fig. 9(a)–(d). Mean flows around NACA0012 profile ($\kappa = 0$) are also presented to illustrate the significant influence of shape modification, especially on the size and position of

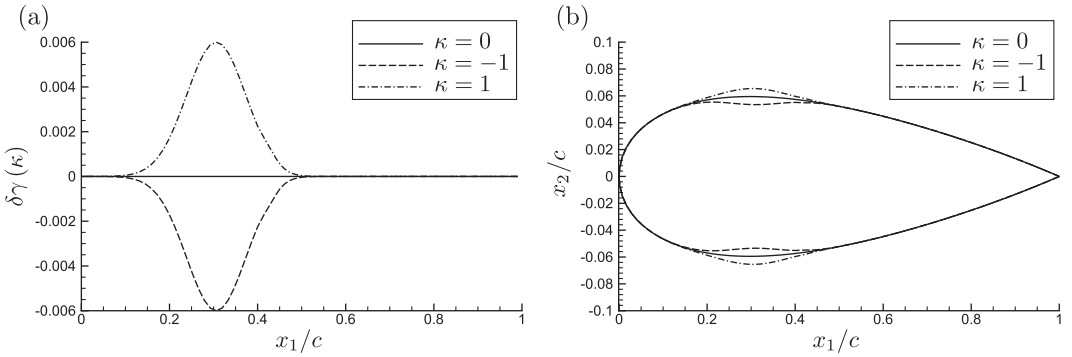

Fig. 8. (a) Normal shape deformation along airfoil chord for three values of κ and (b) corresponding airfoil profiles.

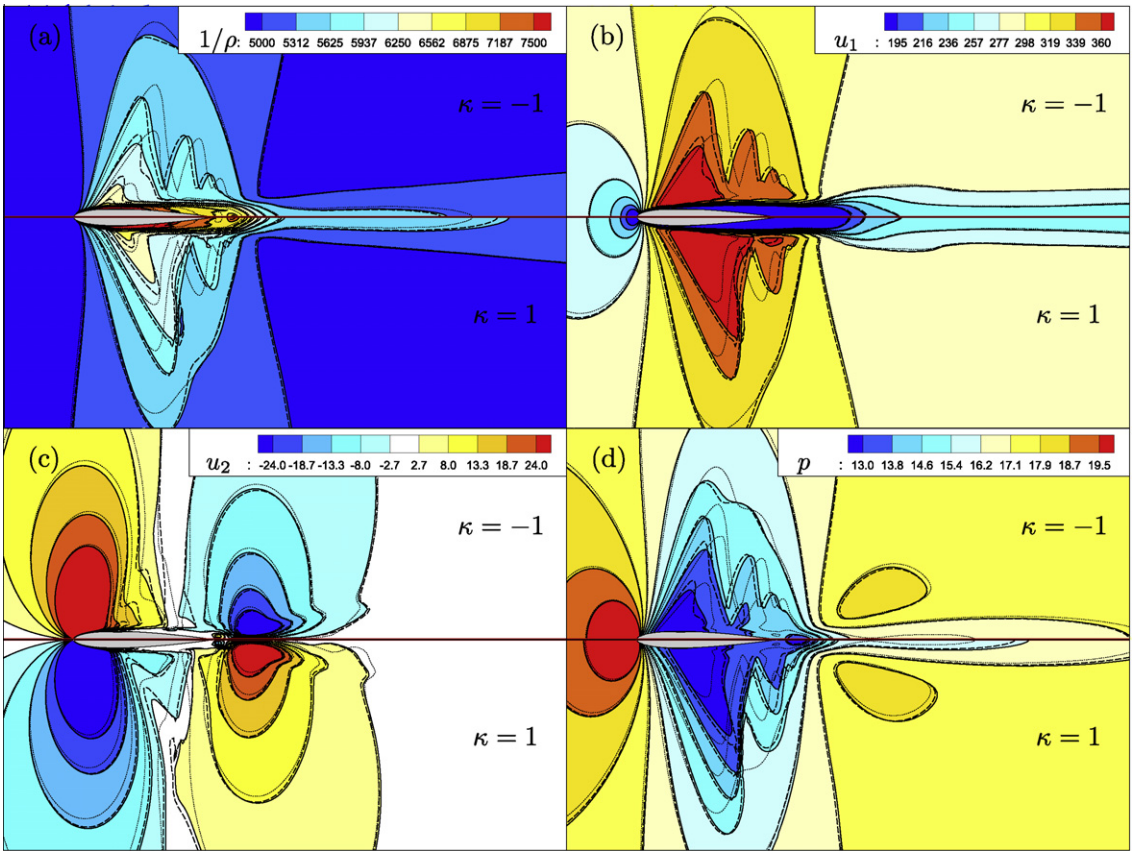

Fig. 9. Mean fields of the state variables: (a) $1/\rho$ (m^3/kg), (b) u_1 (m/s), (c) u_2 (m/s) and (d) p (Pa); NS simulation (bold plain iso-lines and contours), H simulation (bold dashed iso-lines) and NACA0012 ($\kappa = 0$) simulation (thin dashed iso-lines), for $\kappa = -1$ (upper part) and $\kappa = 1$ (lower part).

the supersonic pockets, even if the deformation is moderate. The same type of comparison between instantaneous fields is shown in Fig. 10. For comparison purpose, the fields are phased according to the minimum streamwise velocity signal at point $(x_1/c, x_2/c) = (2.12, 0.05)$. A good agreement is achieved between mean and instantaneous results issued from NS and H approaches.

The relative error between fields issued from NS and H approaches is quantified as follows on Ω^T which is the part of the spatial domain that is not affected by grid deformation ($x_1/c \geqslant 1$), for each variable w_i and for the whole state vector in modified formulation (9):

$$E^{\mathrm{H}}(w_i,\delta\gamma) = \sqrt{\frac{\int_{\Omega^T}\left(w_i^{\mathrm{NS}}(\delta\gamma) - w_i^{\mathrm{H}}(\delta\gamma)\right)^2 d\boldsymbol{x}}{\int_{\Omega^T} w_i^{\mathrm{NS}}(\delta\gamma)^2 d\boldsymbol{x}}} \quad \text{and} \quad E_G^{\mathrm{H}}(\boldsymbol{w},\delta\gamma) = \frac{\|\boldsymbol{w}^{\mathrm{NS}}(\delta\gamma) - \boldsymbol{w}^{\mathrm{H}}(\delta\gamma)\|_{\Omega^T}}{\|\boldsymbol{w}^{\mathrm{NS}}(\delta\gamma)\|_{\Omega^T}}, \tag{39}$$

where, as previously, $\cdot^{\mathrm{NS}}$ and $\cdot^{\mathrm{H}}$ denote fields issued from NS and H simulations respectively. The subdomain Ω^T is considered to avoid interpolations and hazardous estimations in non-overlapping regions. The spatial inner product inducing norm $\|\cdot\|_{\Omega^T}$ is defined as (5) but on Ω^T and considering a generalized expression for σ_i^2 that will be specified in next section (41). These errors concerning mean and instantaneous (same phased fields as in Fig. 10) fluctuating flows are reported in Table 1. In both deformed cases, error levels remain satisfactory. Lower error levels are observed in $\kappa = -1$ case as expected, since this deformation induces smaller changes in flow pattern than $\kappa = 1$ one.

In Fig. 11, relative error $E_G^{\mathrm{H}}(\tilde{\boldsymbol{w}},\delta\gamma)$ is monitored over one von Kármán vortex shedding cycle, starting from the previous phased fields. Both deformations of interest only induce small modifications of the vortex shedding fundamental frequency. Strouhal number varies from St = 1.288 ($\kappa = 1$) to St = 1.364 ($\kappa = -1$). The relative prediction errors of this frequency between NS and H simulations are 0.90% and < 0.01% for cases $\kappa = 1$ and $\kappa = -1$ respectively. The slow growth of the instantaneous error in case $\kappa = 1$ (Fig. 11) is thus due to the slight over-estimation of the Strouhal number. To illustrate airfoil deformation effects, the unsteady lift coefficients issued from NS and NACA0012 profile simulations are plotted in Fig. 12, as well as the lift coefficient issued from H simulation in case $\kappa = 1$. In this latest case, state variables have been interpolated to map the boundary of the deformed profile. The lift coefficient is rigorously simulated by H approach. The relative error on lift oscillation amplitude is 1.12% whereas deformation $\kappa = 1$ induces an amplitude increase of more than 35% compared with $\kappa = 0$ profile.

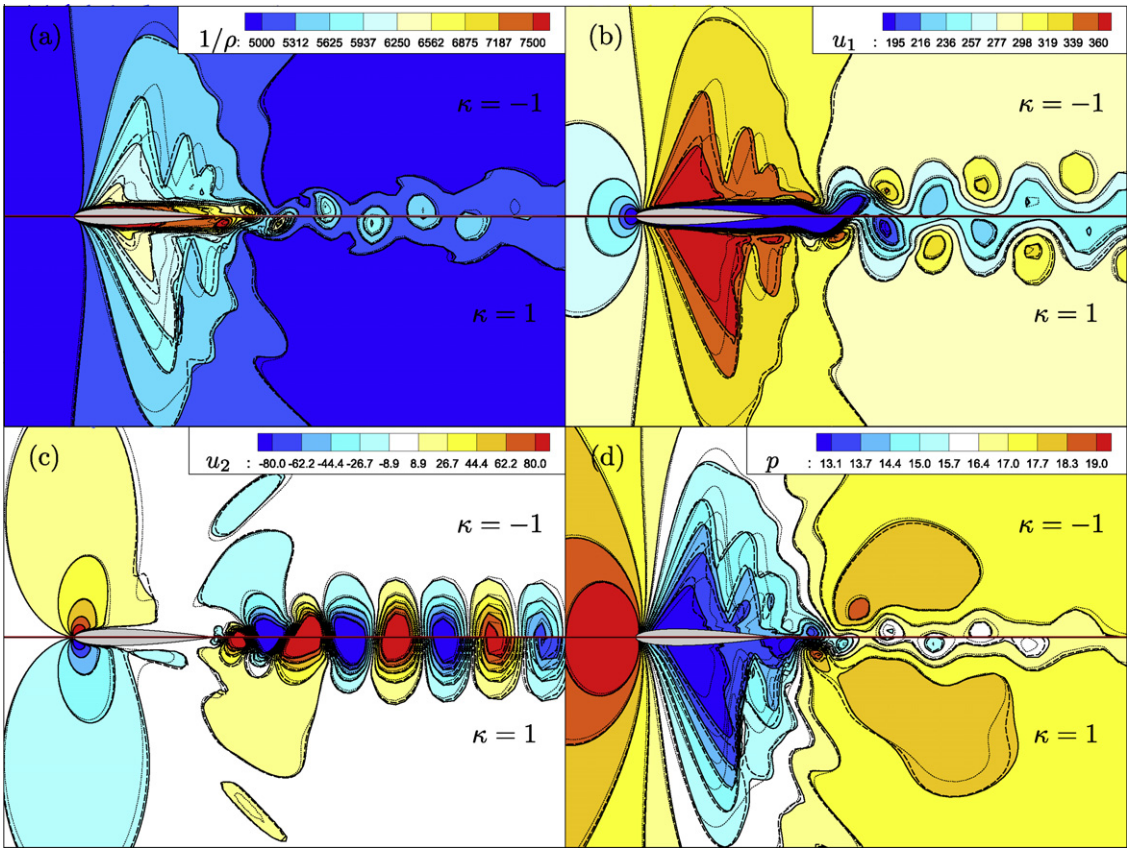

Fig. 10. Same as Fig. 9 concerning phased fields.

Table 1
Prediction errors induced by the use of the fictitious boundary conditions instead of domain deformation.

κ	Field	$E^{\mathrm{H}}(1/\rho,\delta\gamma)\%$	$E^{\mathrm{H}}(u_1,\delta\gamma)\%$	$E^{\mathrm{H}}(u_2,\delta\gamma)\%$	$E^{\mathrm{H}}(p,\delta\gamma)\%$	$E^{\mathrm{H}}_G(\boldsymbol{w},\delta\gamma)\%$
1	$\overline{\boldsymbol{w}}$	0.09	0.11	3.76	0.09	0.09
1	$\tilde{\boldsymbol{w}}$	15.57	13.47	12.28	15.54	14.31
−1	$\overline{\boldsymbol{w}}$	0.03	0.05	3.21	0.03	0.03
−1	$\tilde{\boldsymbol{w}}$	6.86	4.18	3.08	8.00	5.79

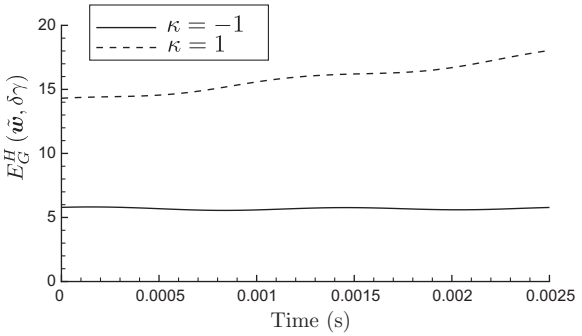

Fig. 11. Instantaneous prediction error of state vector fluctuation $E^{\mathrm{H}}_G(\tilde{\boldsymbol{w}},\delta\gamma)$ as a function of time.

The fictitious boundary conditions derived from the Hadamard formulation mimic efficiently airfoil profile deformations of moderate amplitudes, without any modification of the computational domain. In next section, HF simulations carried out by means of this fictitious domain deformation technique are used to build a ROM sensitive to airfoil deformation.

5. Reduced-order modeling of transonic flow around a deformed airfoil

The previously described low-dimensional modeling approach (Section 3) is extended to handle airfoil shape deformations introduced at HF level through the Hadamard formulation described in Section 4. Three main points have to be addressed:

- How to define a POD basis valid for a certain range of shape deformations?
- How to introduce airfoil deformation in the ROM?
- How to calibrate the ROM in this context?

Section 5.1 focuses on the first point and Section 5.2 on the two following ones. A procedure based on a single mixed POD basis and on a forcing of the ROM by appropriate control functions is put forward. The corresponding ROM is applied in Section 5.3 and its reliability towards shape deformation is examined.

5.1. Mixed POD basis

Two different approaches are generally considered concerning POD in the context of parametric studies: single basis a priori valid on the whole parameter space of interest [e.g. 24,27] or adaptive basis [19,47,59–61]. The present study focuses on shape deformations that do not lead to strong modifications in flow topology. Therefore, a single POD basis is retained. However, the approach suggested here could be integrated directly in a basis adaption procedure like for example Trust-Region POD algorithm [59].

In the following, all HF simulations around deformed airfoils are issued from the previously validated Hadamard formulation (H simulations in Section 4.2) on reference domain Ω_0. For more simplicity in POD ROM presentation, the considered perturbation $\delta\gamma$ depends on a single shape parameter κ. This does not alter the generality of the suggested framework since extension to multiple shape parameters is straightforward. The state vector associated with deformation $\delta\gamma(\kappa)$ and expressed in modified formulation (9) is denoted by $\boldsymbol{w}(\boldsymbol{x},t,\kappa)=\boldsymbol{w}(\delta\gamma(\kappa))(\boldsymbol{x},t)$, for $\boldsymbol{x}\in\Omega_0$, since the Hadamard formulation is considered. Its fluctuation is denoted by $\tilde{\boldsymbol{w}}(\boldsymbol{x},t,\kappa)=\boldsymbol{w}(\boldsymbol{x},t,\kappa)-\overline{\boldsymbol{w}}(\boldsymbol{x},\kappa)$, where $\overline{\boldsymbol{w}}$ is the corresponding space/shape-dependent mean state.

For each profile $\kappa=\{-1,0,1\}$, the statistical content $I_{N_{\mathrm{pod}}}$ (25) extracted by the previous POD basis built from $\kappa=0$ snapshot series are plotted in Fig. 13(a)–(c). In all cases, snapshot series are composed of $N_t=100$ samples collected over one period of the von Kármán vortex shedding. In cases $\kappa=-1$ and $\kappa=1$, the statistical content conveyed by POD bases issued from

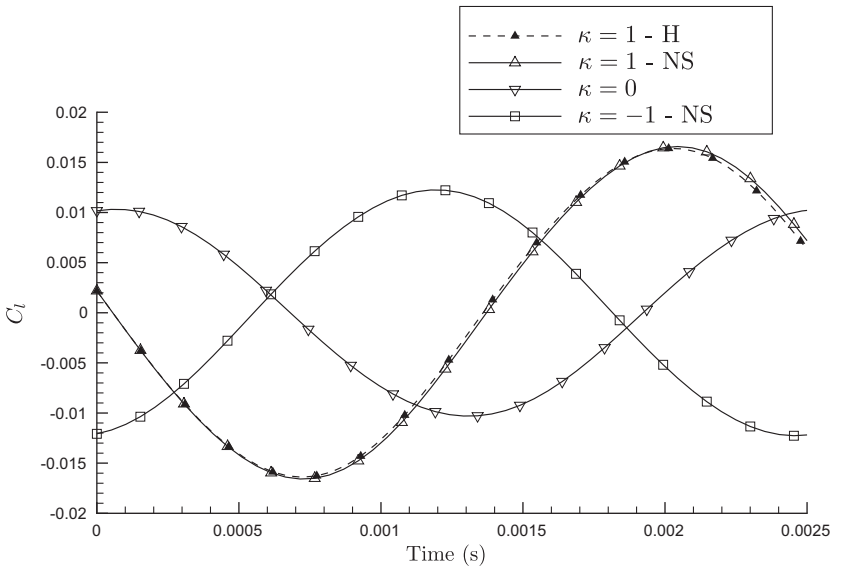

Fig. 12. Unsteady lift coefficients issued from HF simulations around NACA0012 profile and deformed profiles by NS approach, and by H approach in case $\kappa = 1$. The signals have been phased for comparison purpose in case $\kappa = 1$.

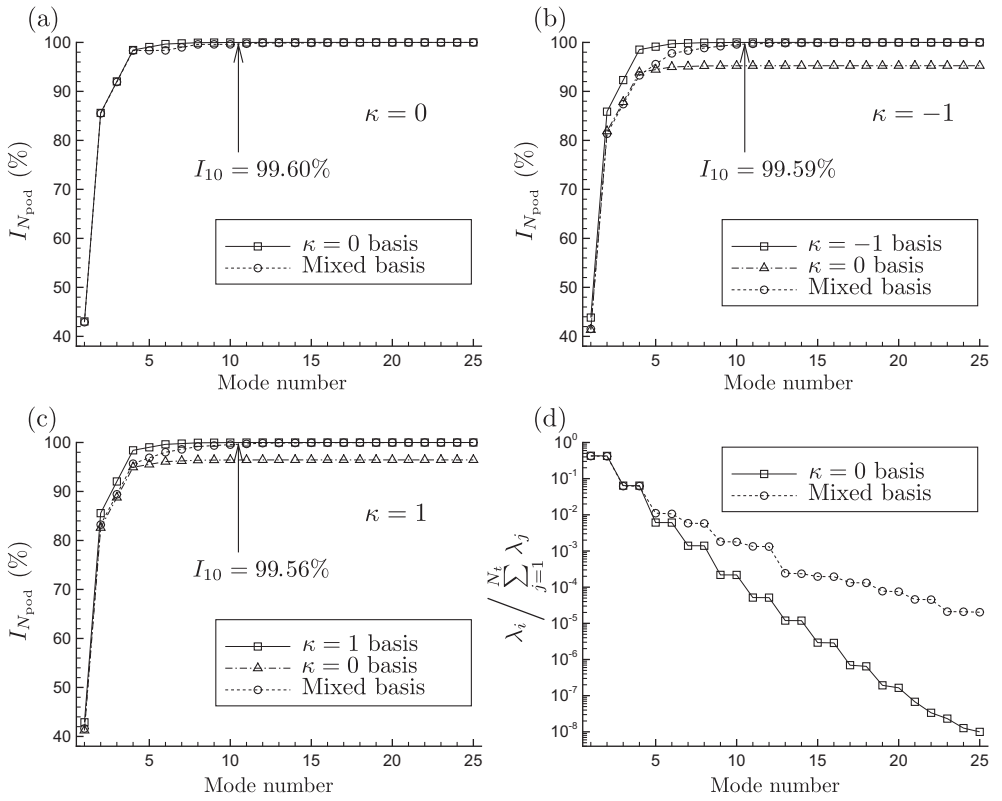

Fig. 13. (a)–(c) Relative statistical content of the truncated POD basis as a function of mode number, for snapshots collected in configuration: (a) $\kappa = 0$, (b) $\kappa = -1$ and (c) $\kappa = 1$. In (b) and (c) the relative statistical content captured by $\kappa = 0$ basis is plotted for comparison purpose. (d) Relative statistical content of each POD mode: $\kappa = 0$ basis and mixed $\kappa = \{-1, 0, 1\}$ basis.

$\kappa = -1$ and $\kappa = 1$ snapshot series respectively are also plotted, for comparison purpose. In the two deformed configurations, $\kappa = 0$ POD basis fails in capturing all snapshot variance, even if the number of modes is increased.

To extract a higher level of statistical content from several snapshot series with a single basis, POD procedure can be extended by replacing time-averaging operator in (6) by the following, for any time/shape-dependent quantity $q(t,\kappa)$ and N_s shapes:

$$\lfloor q \rfloor = \frac{1}{N_s}\sum_{i=1}^{N_s}\langle q(\cdot,\kappa_i)\rangle. \tag{40}$$

Time/shape-averaging operator is thus denoted by $\lfloor\cdot\rfloor$ and time-averaging operator by $\langle\cdot\rangle$. An extension towards continuously distributed shape case is straightforward by replacing discrete summation in (40) by an integration over continuous κ.

The averaged statistical variance involved in the inner product (5) is extended as follows:

$$\sigma_i^2 = \int_{\Omega_0} \lfloor \tilde{w}_i^2 \rfloor d\boldsymbol{x}. \tag{41}$$

'Snapshot-POD' technique thus consists in finding the eigenfunctions of time/shape correlation tensor $K(t,t',\kappa_i,\kappa_j) = (\tilde{\boldsymbol{w}}(\cdot,t,\kappa_i),\tilde{\boldsymbol{w}}(\cdot,t',\kappa_j))_{\Omega_0}$:

$$\lfloor K(t,\cdot,\kappa_i,\cdot)\psi_k \rfloor_{(t',\kappa_j)} = \lambda_k \psi_k(t,\kappa_i) \quad \text{with} \quad \lfloor \psi_i \psi_j \rfloor = \delta_{ij}, \tag{42}$$

$$\text{and} \quad \boldsymbol{\Phi}_i(\boldsymbol{x}) = \frac{1}{\sqrt{\lambda_i}} \lfloor \tilde{\boldsymbol{w}}(\boldsymbol{x},\cdot,\cdot)\psi_i \rfloor \quad \text{for } \lambda_i > 0. \tag{43}$$

In (42), subscript $\cdot_{(t',\kappa_j)}$ indicates that the integration involves the second time and shape variables of K while t and κ_i are fixed.

POD temporal coefficients are thus shape-dependent while spatial POD modes are not:

$$\boldsymbol{w}(\boldsymbol{x},t,\kappa) \approx \overline{\boldsymbol{w}}(\boldsymbol{x},\kappa) + \sum_{i=1}^{N_{\text{pod}}} a_i(t,\kappa)\boldsymbol{\Phi}_i(\boldsymbol{x}). \tag{44}$$

The statistical contents conveyed by the mixed POD basis (43) that includes information from $\kappa = \{-1,0,1\}$ snapshot series are plotted in Fig. 13(a)–(c). Each $I_{N_{\text{pod}}}$ presented in these figures involves the same extended definition of σ_i^2 (41) in the inner product. It can be observed that if 10 modes are retained, the conveyed statistical content in each configuration is close to the statistical content conveyed by a dedicated POD basis, as shown in Fig. 13(a)–(c). This number of modes is considered in the following. The spectrum associated with the mixed basis is less steep than $\kappa = 0$ basis one (Fig. 13(d)). This means that the role played by higher index modes is increased when vortex shedding pattern modifications that are induced by airfoil deformation have to be captured by a single spatial basis.

5.2. Airfoil deformation in ROM

Considering expansion (44) along with mixed POD modes (43), a ROM is built as described in Section 3.2. In this ROM, shape deformation only appears through the mean flow $\overline{\boldsymbol{w}}(\boldsymbol{x},\kappa)$, which can be regarded as a forcing term or a control function [24] of the dynamical system. As a forcing term, the mean flow has to be known and if it is not, it must be estimated. In the present study, two different approaches are suggested to evaluate the control function in not previously HF-resolved configurations, from known flows. The first one consists in introducing an actuation function that is a linear function of shape parameter. This actuation function involves an actuation mode $\boldsymbol{\Phi}^a$ that is called 'deformation mode' in the following. The statistical approach suggested in flow control context in [62,63] can be adapted to the present problem. The control function is defined by:

$$\hat{\boldsymbol{w}}_1(\boldsymbol{x},\kappa) = \overline{\boldsymbol{w}}(\boldsymbol{x},0) + \kappa\boldsymbol{\Phi}^a(\boldsymbol{x}). \tag{45}$$

The deformation mode is the function that best represents, in average, the part of the dataset that is not captured by the truncated POD basis, the whole dataset being centered about $\overline{\boldsymbol{w}}(\boldsymbol{x},0)$:

$$\boldsymbol{\Phi}^a = \arg\min_{\boldsymbol{\Psi}} \lfloor \|J(\cdot,\cdot,\cdot,\boldsymbol{\Psi})\|_{\Omega_0}^2 \rfloor \quad \text{with} \quad J(\boldsymbol{x},t,\kappa,\boldsymbol{\Psi}) = \breve{\boldsymbol{w}}(\boldsymbol{x},t,\kappa) - \kappa\boldsymbol{\Psi}(\boldsymbol{x}) \tag{46}$$

and

$$\breve{\boldsymbol{w}}(\boldsymbol{x},t,\kappa) = \boldsymbol{w}(\boldsymbol{x},t,\kappa) - \overline{\boldsymbol{w}}(\boldsymbol{x},0) - \Pi_{N_{\text{pod}}}(\boldsymbol{w}(\boldsymbol{x},t,\kappa) - \overline{\boldsymbol{w}}(\boldsymbol{x},0)), \tag{47}$$

where $\Pi_{N_{\text{pod}}}$ is the orthogonal projector onto $\text{span}\{\boldsymbol{\Phi}_1,\ldots,\boldsymbol{\Phi}_{N_{\text{pod}}}\}$.

The corresponding mode is [63]:

$$\boldsymbol{\Phi}^a = \frac{\lfloor \kappa\breve{\boldsymbol{w}} \rfloor}{\lfloor \kappa^2 \rfloor}. \tag{48}$$

As reported in [63], this approach can be easily extended to handle multiple shape parameters.

For comparison purpose, an interpolation of known mean flows is also considered to estimate the forcing term. For example, if $\kappa = \{-1, 0, 1\}$ mean flows are known, any intermediate forcing function can be estimated as:

$$\hat{\boldsymbol{w}}_2(\boldsymbol{x}, \kappa) = \overline{\boldsymbol{w}}(\boldsymbol{x}, 0) - \frac{\overline{\boldsymbol{w}}(\boldsymbol{x}, -1) - \overline{\boldsymbol{w}}(\boldsymbol{x}, 1)}{2}\kappa + \left(\frac{\overline{\boldsymbol{w}}(\boldsymbol{x}, -1) + \overline{\boldsymbol{w}}(\boldsymbol{x}, 1)}{2} - \overline{\boldsymbol{w}}(\boldsymbol{x}, 0)\right)\kappa^2. \tag{49}$$

In the particular case where $\kappa = \{-1, 0, 1\}$ flows are known, it can be noticed that, if POD basis fails in capturing the shift between mean flows ($\Pi_{N_{\text{pod}}}(\overline{\boldsymbol{w}}(\boldsymbol{x}, \kappa) - \overline{\boldsymbol{w}}(\boldsymbol{x}, 0)) \approx \boldsymbol{0}$, for $\kappa = \{-1, 1\}$), which is generally the case [7], then $\hat{\boldsymbol{w}}_1$ corresponds to the linear part of $\hat{\boldsymbol{w}}_2$.

The calibration procedure presented in Section 3.3 is applied separately to each known configuration with calibration cost threshold $\mathcal{C} = 20\%$. In unknown intermediate cases, the calibration coefficients issued from case $\kappa = 0$ calibration are considered.

5.3. ROM prediction

ROM reliability concerning the prediction of the time/shape-dependent POD coefficients is assessed for HF-resolved and unknown configurations.

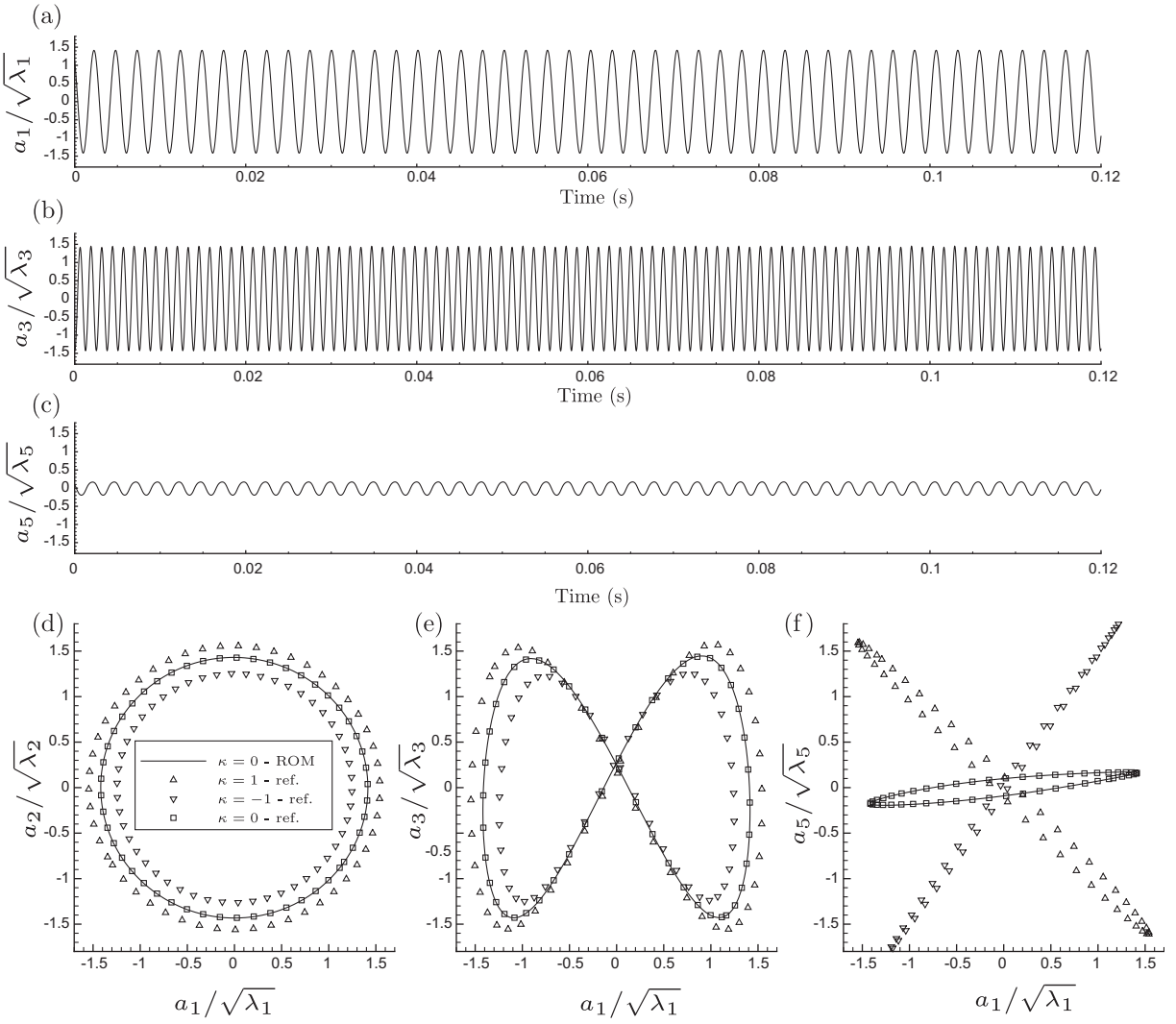

Fig. 14. Selected POD temporal coefficients in case $\kappa = 0$: (a)–(c) ROM prediction as a function of time, (d)–(f) reference and ROM prediction in phase diagram. In (d)–(f) ROM prediction is plotted after convergence on limit cycle is reached.

5.3.1. HF-resolved flows

Three configurations are assumed to be known by HF Hadamard simulation ($\kappa = \{-1, 0, 1\}$). The corresponding snapshot series are used to extract POD modes as previously detailed (43). In each case, the ROM is forced by the exact known mean flow and the calibration coefficients used are those determined independently for each configuration ($\kappa = 0$, $\kappa = -1$ or $\kappa = 1$). In Figs. 14–16, selected temporal coefficients predicted by the ROM (a^{rom}) are shown as functions of time and in phase diagram, for each known case. The same initial condition ($a_i^{\mathrm{pod}}(0,0) = (\tilde{\boldsymbol{w}}(\cdot,0,0), \boldsymbol{\Phi}_i)_{\Omega_0}$) is considered for all ROM integrations. From this initial condition, the integration is performed over more than 40 vortex shedding cycles. As shown in Figs. 14–16(a)–(c), the predicted dynamics are stable and converge towards periodic oscillations. The phase diagrams in Figs. 14–16(d)–(f) depict predicted coefficients once the periodic regime is reached. For comparison purpose, the reference temporal coefficients associated with known flows ($a^{\mathrm{pod}}(t,\kappa) = (\tilde{\boldsymbol{w}}(\cdot,t,\kappa), \boldsymbol{\Phi}_i)_{\Omega_0}$) are also plotted (symbols). It can be observed that airfoil deformation induces significant modulations of POD temporal coefficients. In all three known configurations, forced ROMs achieve reliable predictions of reference temporal coefficients. In Figs. 15 and 16, the temporal coefficients issued from ROMs forced by exact mean flows but where calibration coefficients are those evaluated in case $\kappa = 0$ are also presented (ROM_0, dashed line). Satisfactory predictions are achieved by these ROMs that are only driven by the forcing term. This point illustrates the sensitivity of the dynamical system towards control function and the fact that this sensitivity is not inhibited by calibration procedure.

The relative prediction error of each POD mode energy level and the instantaneous prediction error of POD temporal coefficients are defined as follows:

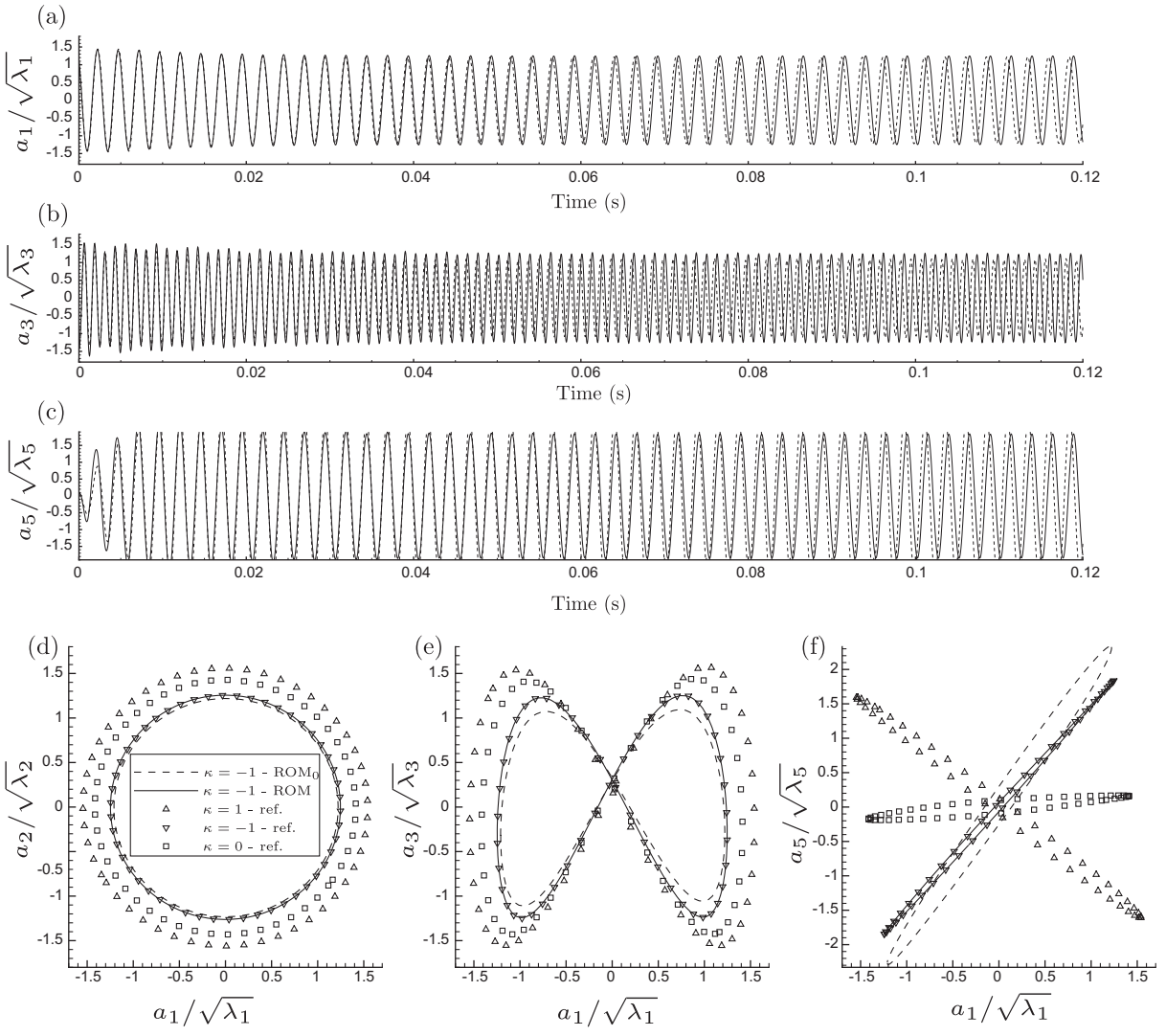

Fig. 15. Same as Fig. 14 in case $\kappa = -1$. In ROM_0, calibration coefficients are those determined in case $\kappa = 0$.

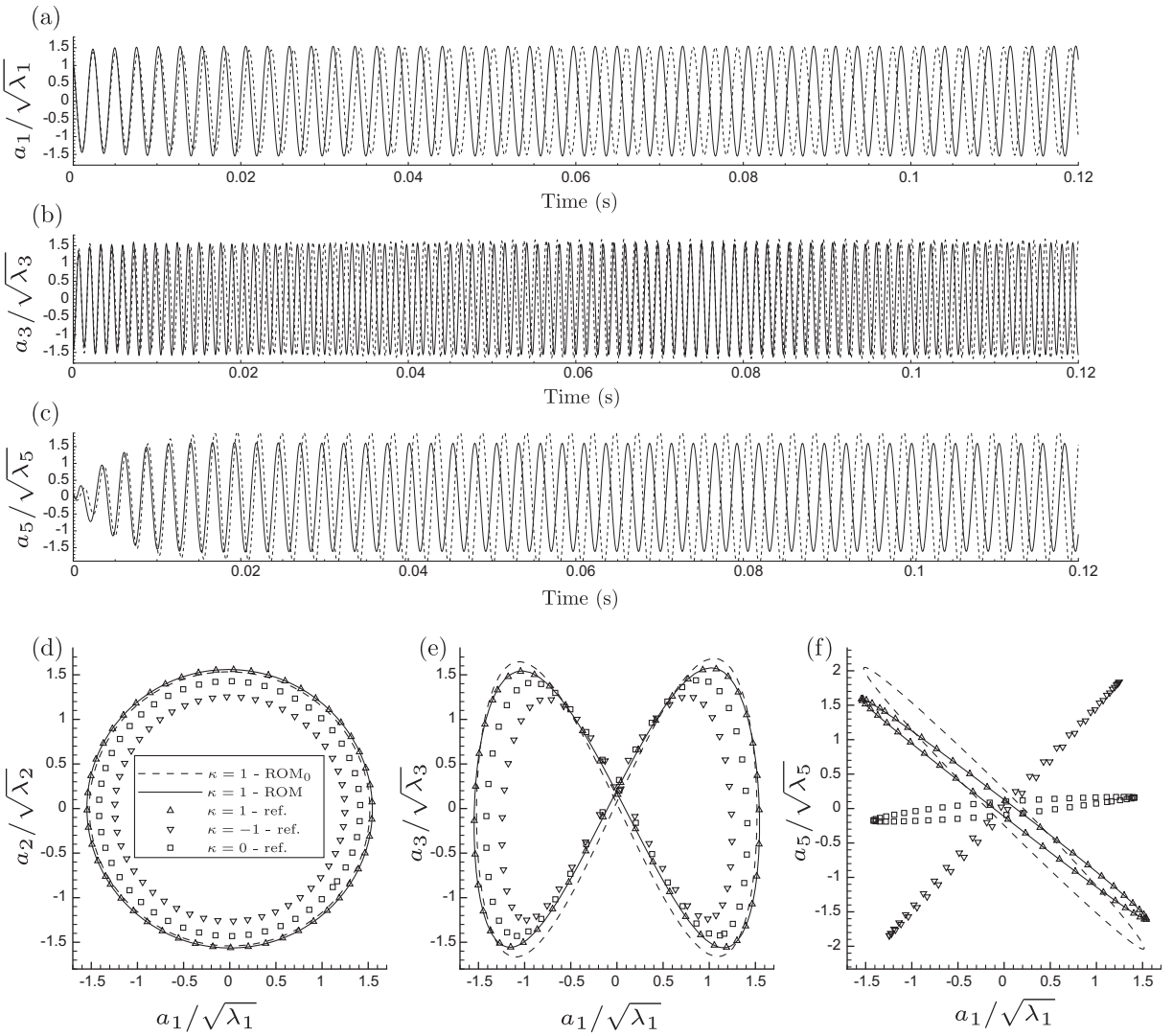

Fig. 16. Same as Fig. 15 in case $\kappa = 1$.

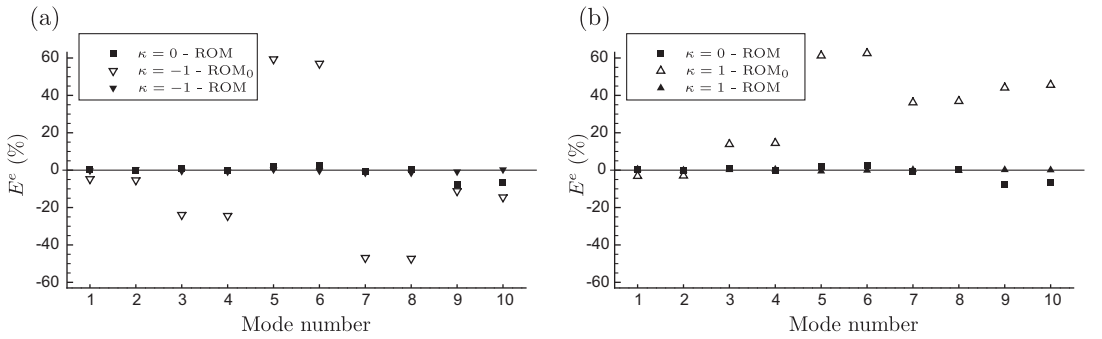

Fig. 17. Relative error of POD mode energy levels predicted by ROM.

$$E^e(i,\kappa) = \frac{\langle (a_i^{\text{rom}}(\cdot,\kappa))^2 \rangle - \langle (a_i^{\text{pod}}(\cdot,\kappa))^2 \rangle}{\langle (a_i^{\text{pod}}(\cdot,\kappa))^2 \rangle}, \quad E^R(t,\kappa) = \sqrt{\frac{\sum_{i=1}^{N_{\text{pod}}} \left(a_i^{\text{rom}}(t,\kappa) - a_i^{\text{pod}}(t,\kappa) \right)^2}{\sum_{i=1}^{N_{\text{pod}}} \left(a_i^{\text{pod}}(t,\kappa) \right)^2}}, \tag{50}$$

where, as previously, a_i^{pod} and a_i^{rom} denote reference and predicted temporal coefficients respectively. As shown in Fig. 17, the energy levels of POD modes are accurately estimated by the ROM when dedicated calibration coefficients are used. When the calibration coefficients related to case $\kappa = 0$ are used in cases $\kappa = \{-1, 1\}$ (ROM_0), satisfactory predictions are achieved, as depicted qualitatively in Figs. 15 and 16.

In Fig. 18, instantaneous errors E^R (50) are plotted for predicted coefficients issued from ROM ($\kappa = \{-1, 0, 1\}$) and ROM_0 ($\kappa = \{-1, 1\}$). For comparison purpose, reference and predicted signals have been phased. The prediction error remains small in all cases when the corresponding calibration coefficients are used (ROM) and moderate when only $\kappa = 0$ calibration coefficients are considered (ROM_0). The slow growth of the error observed in case $\kappa = 1$ (ROM_0, Fig. 18(b)), is induced by a slight under-estimation of vortex shedding frequency.

In spite of the limited effect of shape deformation on Strouhal number, the prediction of the fundamental frequency can be monitored. The predicted Strouhal numbers and relative errors compared with HF simulations are reported in Table 2. Even if a lower precision is achieved when calibration coefficients issued from case $\kappa = 0$ are used in deformed configurations ($\kappa = \{-1, 1\}$), the prediction error remains small.

The present analysis shows that better predictions are achieved when the dedicated calibration coefficients are used. The differences observed between ROM and ROM_0 accuracies emphasize the dependency of the calibration coefficients on the shape parameter κ. The development of an adaptive calibration procedure that would provide a relationship between κ and the calibration coefficients is a challenging issue that is beyond the objectives of the present work. The present study shows that a satisfactory prediction of the predominant features of the transonic unsteady flow past an airfoil can be achieved by considering calibration coefficients associated with a reference case (here $\kappa = 0$), in the neighborhood of the configuration of interest. In particular, the first POD temporal coefficients which convey most of the system statistical content are accurately predicted. As mentioned previously, this emphasizes ROM sensitivity to forcing term, independently of calibration procedure. This is an important point for the prediction of configurations not resolved by HF model, as discussed in Section 5.3.2.

To illustrate ROM predictive capacities concerning the physical variables, the unsteady lift coefficients issued from HF and low-dimensional approaches in case $\kappa = 1$ are shown in Fig. 19. ROM prediction matches accurately HF signal and ROM_0 prediction is also in good agreement. The relative errors concerning lift oscillation amplitude are 0.02% (ROM) and 2.45% (ROM_0).

5.3.2. Unknown flow

ROM reliability concerning the prediction of flows not previously resolved by HF model is examined in the intermediate case $\kappa = 0.5$. As in previous cases, the statistical content extracted by the $\kappa = \{-1, 0, 1\}$ mixed POD basis from centered

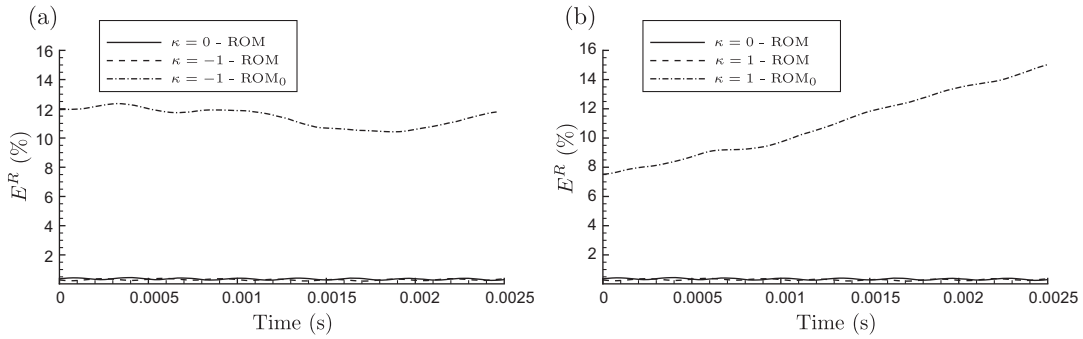

Fig. 18. Instantaneous prediction error of POD temporal coefficients as a function of time. Phased signals once limit cycle is reached.

Table 2
Prediction of the von Kármán vortex shedding frequency by ROM and relative error compared with HF simulation.

Shape-κ	Forcing function	Calibration-κ	Strouhal number	Relative error w.r.t. HF (%)
0	$\overline{\boldsymbol{w}}(\boldsymbol{x}, 0)$	0	1.342	0.15
−1	$\overline{\boldsymbol{w}}(\boldsymbol{x}, -1)$	0	1.370	0.47
−1	$\overline{\boldsymbol{w}}(\boldsymbol{x}, -1)$	−1	1.364	0.03
1	$\overline{\boldsymbol{w}}(\boldsymbol{x}, 1)$	0	1.280	1.48
1	$\overline{\boldsymbol{w}}(\boldsymbol{x}, 1)$	1	1.299	0.02
0.5	$\overline{\boldsymbol{w}}(\boldsymbol{x}, 0.5)$	0	1.297	1.85
0.5	$\hat{\boldsymbol{w}}_1(\boldsymbol{x}, 0.5)$	0	1.298	1.78
0.5	$\hat{\boldsymbol{w}}_2(\boldsymbol{x}, 0.5)$	0	1.299	1.70
0.5	$\overline{\boldsymbol{w}}(\boldsymbol{x}, 0.5)$	0.5	1.322	0.02
0.5	$\hat{\boldsymbol{w}}_1(\boldsymbol{x}, 0.5)$	0.5	1.323	0.08
0.5	$\hat{\boldsymbol{w}}_2(\boldsymbol{x}, 0.5)$	0.5	1.323	0.07

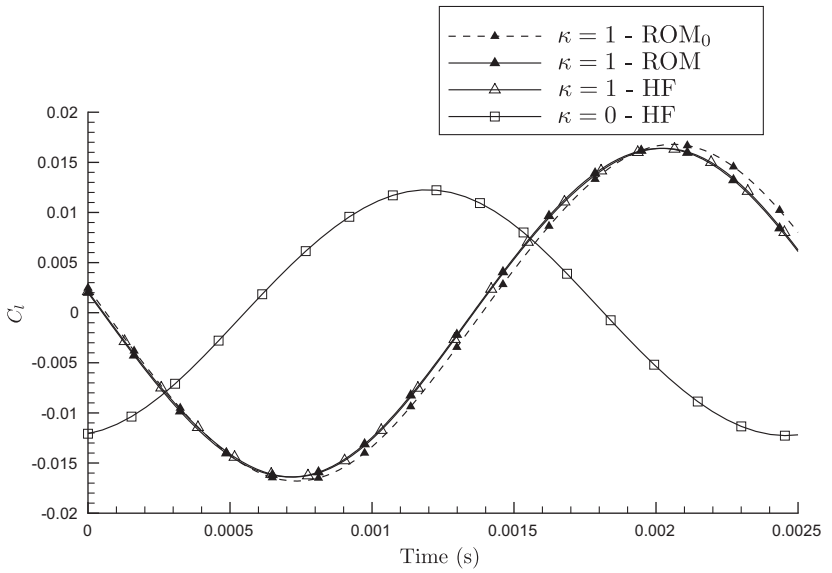

Fig. 19. Unsteady lift coefficients of reference and deformed airfoils. The signals have been phased for comparison purpose in case $\kappa = 1$.

snapshot series is monitored (Fig. 20). The conveyed statistical content in this intermediate case is similar to previous cases (see Fig. 13(a)–(c)). It is recalled that $\kappa = 0.5$ snapshots are not utilized to build POD basis in this intermediate case.

In the following, two levels of knowledge are considered concerning the forcing term in case $\kappa = 0.5$. The first level assumes that the mean flow is known and thus it can be used as a forcing term in the ROM. In the second level, the mean flow has to be estimated as previously described. The deformation mode $\mathbf{\Phi}^a$ issued from $\kappa = \{-1, 0, 1\}$ snapshot series is shown in Fig. 21. Approximations of the mean flow according to (45) and (49) are both in good agreement with the exact mean flow, the relative error E_G^H (39) is lower than 0.02% in both cases.

As a first step, to assess the efficiency of the mean field approximations as forcing terms, the calibration coefficients used are those determined in case $\kappa = 0.5$ (ROM). The relative error of POD mode energy levels evaluated once the periodic regime is reached are small for the three forcing approaches, as shown in Fig. 22(a). Both mean field approximations lead to very similar results and do not modify significantly ROM accuracy compared to $\overline{\boldsymbol{w}}$. A small difference can be noticed for modes 5 and 6 where $\hat{\boldsymbol{w}}_1$ leads to slightly more accurate predictions than $\hat{\boldsymbol{w}}_2$. The difference observed has no incidence on the instantaneous prediction error (Fig. 23(a)) that is small for the three forcing terms. The vortex shedding frequency is accurately predicted (Table 2) as well as the unsteady lift coefficient, compared to HF simulation (Fig. 24(a)). The relative error of lift oscillation amplitude is lower than 0.4% for the three forcing terms. Therefore the mean field can be replaced by its approximations without altering ROM accuracy, in the present intermediate case where the dedicated calibration coefficients are known.

In the case of an intermediate configuration not resolved by HF model, the dedicated calibration coefficients are generally not known. In the following, the calibration coefficients used are those determined in case $\kappa = 0$. The corresponding ROM is referred to as ROM$_0$, as previously. In Figs. 25 and 26, selected temporal coefficients issued from ROM$_0$ forced by $\overline{\boldsymbol{w}}$ and $\hat{\boldsymbol{w}}_1$ are presented. For comparison purpose, the reference coefficients plotted in Fig. 26(d)–(f) (circles) are the projections of

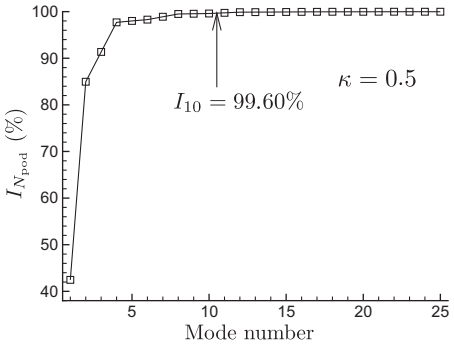

Fig. 20. Relative statistical content of the truncated mixed POD basis as a function of mode number in case $\kappa = 0.5$.

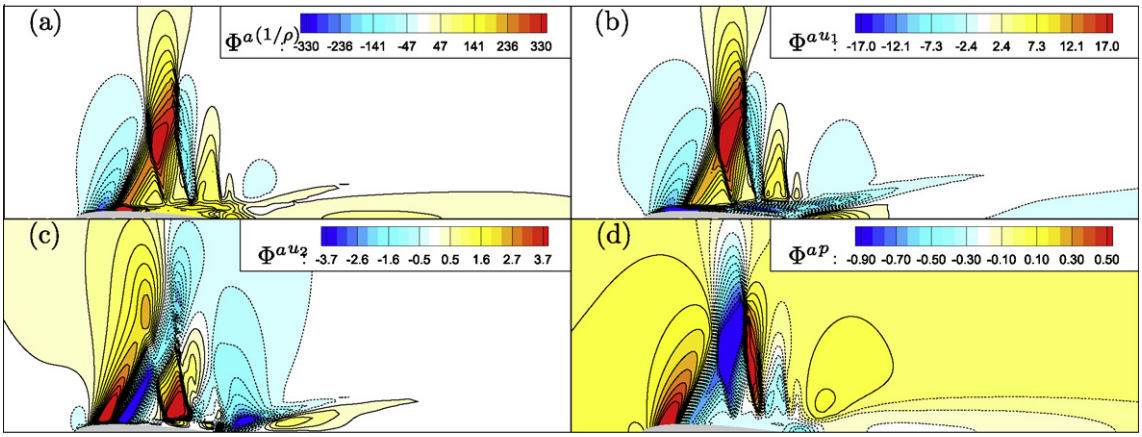

Fig. 21. Actuation mode associated with: (a) $1/\rho$ (m^3/kg), (b) u_1 (m/s), (c) u_2 (m/s) and (d) p (Pa). The upper side of the domain is presented. Dashed iso-lines denote negative iso-contours.

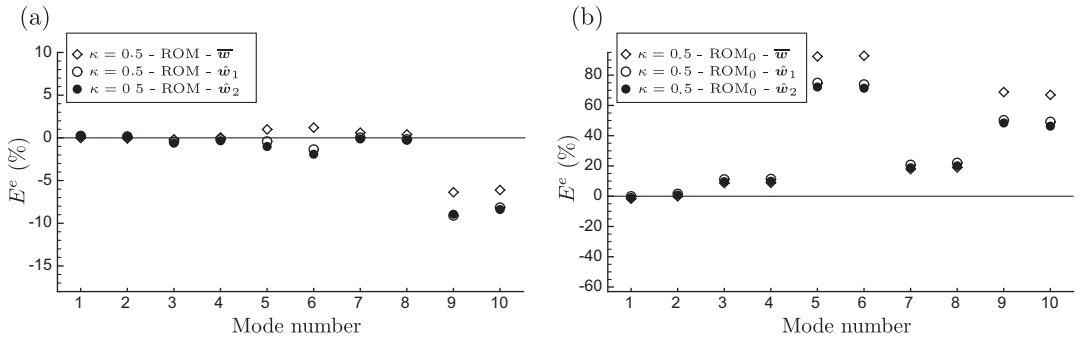

Fig. 22. Same as Fig. 17 in case $\kappa = 0.5$.

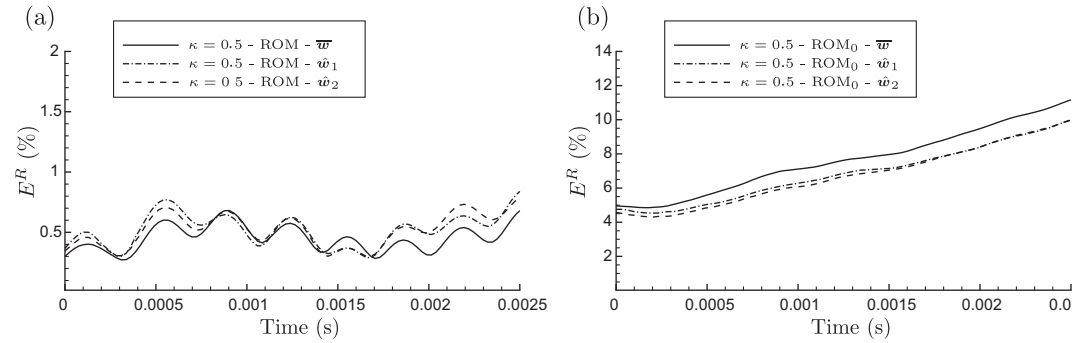

Fig. 23. Same as Fig. 18 in case $\kappa = 0.5$.

snapshot series centered about the approximated mean field $\hat{\boldsymbol{w}}_1$. As shown quantitatively in the following, both mean field approximations yield very close results and thus only temporal coefficients related to $\hat{\boldsymbol{w}}_1$ forcing are qualitatively presented here.

The predicted temporal coefficients converge towards periodic oscillations as in previous cases. A satisfactory comparison is achieved between predicted and reference coefficients in phase diagrams. The relative error of POD mode energy levels (Fig. 22(b)) confirms in particular the efficient prediction of the first four temporal coefficients, that are responsible for most of the system statistical content. Similar predictions are achieved when considering $\overline{\boldsymbol{w}}$, $\hat{\boldsymbol{w}}_1$ and $\hat{\boldsymbol{w}}_2$ as forcing terms, as shown previously in the case where the dedicated calibration coefficients are known (Fig. 22(a)). This is confirmed by monitoring the instantaneous prediction error (Fig. 23(b)). A slight under-estimation of Strouhal number is responsible for the slow

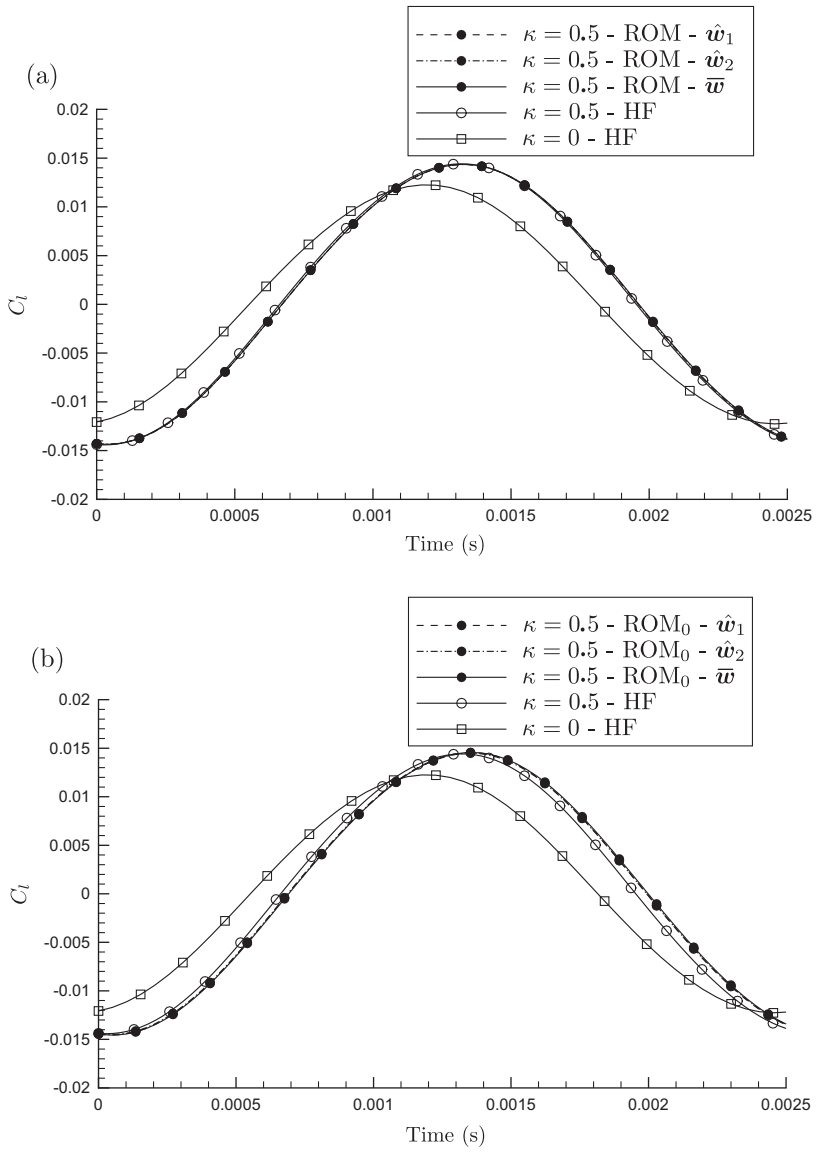

Fig. 24. Same as Fig. 19 in case $\kappa = 0.5$.

growth of this instantaneous error in all cases. The fundamental frequencies predicted in this intermediate case as well as the relative errors compared with HF simulation are reported in Table 2.

The unsteady lift coefficients issued from ROM$_0$ predictions and HF model are plotted in Fig. 24(b). The relative error of oscillation amplitude remains lower than 1% for the three forcing terms, while the deformation $\kappa = 0.5$ induces an increase of more than 15% of this amplitude, compared with case $\kappa = 0$.

The ROM has been applied for the prediction of a flow that was not previously resolved by HF approach. The two suggested approximations of the forcing term yield very similar results compared to the exact mean field. A comparison of ROM and ROM$_0$ predictions shows that the main source of inaccuracy is the calibration procedure and more precisely, the use of the calibration coefficients evaluated in case $\kappa = 0$, as discussed in Section 5.3.1. The reliability of the ROM driven by the exact and approximated mean flows has been quantified. ROM$_0$ achieves an accurate prediction of the predominant features of a completely unknown unsteady transonic flow, as illustrated by the efficient prediction of the lift coefficient.

6. Conclusion

A ROM of the fully compressible Navier–Stokes equations has been proposed for the prediction of unsteady transonic flows past an airfoil submitted to small deformations. This relies on the three following contributions.

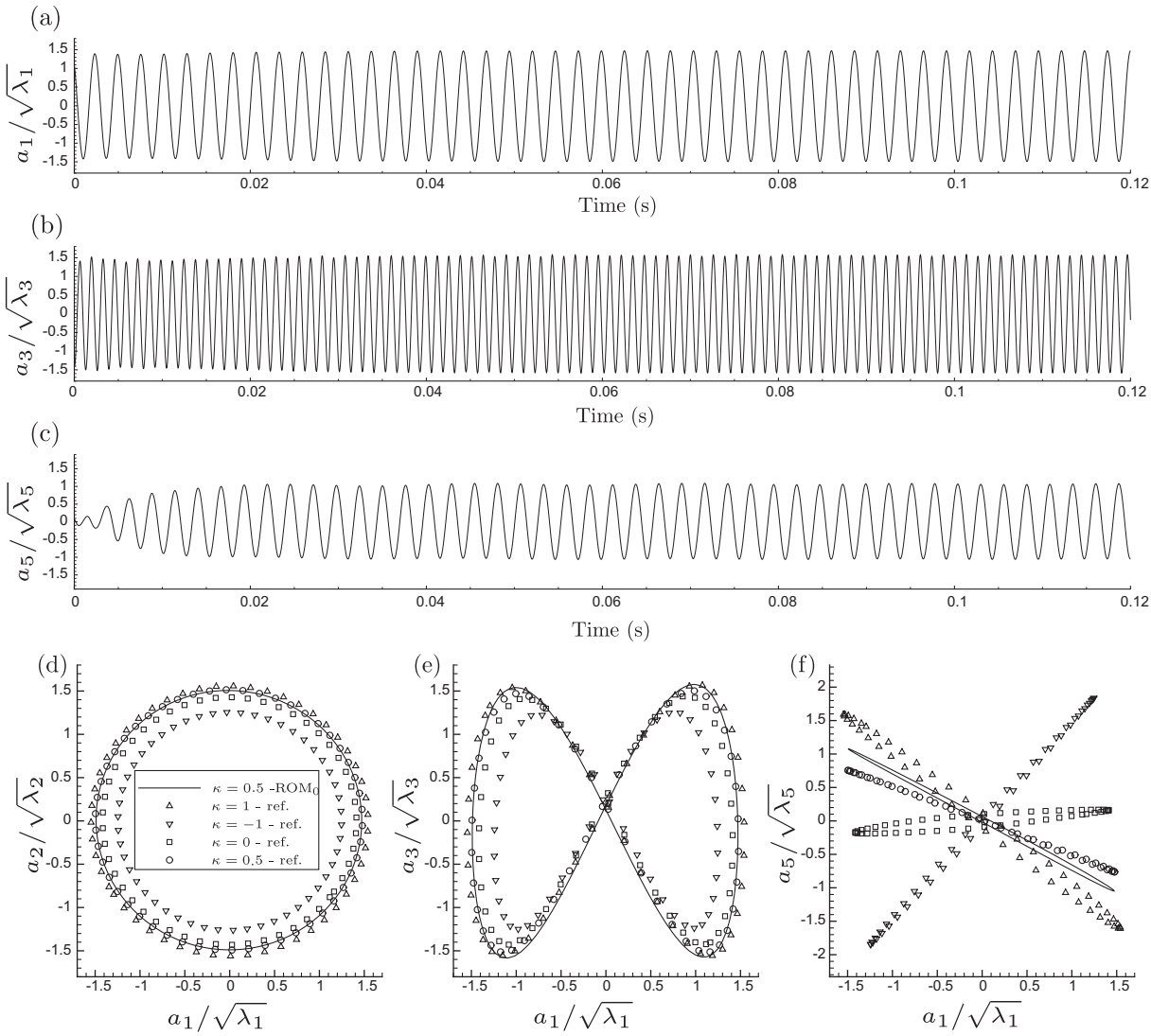

Fig. 25. Same as Fig. 14 in case $\kappa = 0.5$ where mean flow is known.

First, a POD-Galerkin modeling approach has been designed on the basis of a modified state formulation, a consistent inner product and a suitable calibration procedure, leading to a 10-dimensional quadratic ODE system relevant to the prediction of main flow features captured by POD.

Second, on the basis of the Hadamard formulation of HF model, a fictitious domain deformation technique has been suggested. This approach allows to handle small shape perturbations without deforming the reference spatial domain: normal shape perturbations are mimicked by a modification of the conditions on fictitiously deformed boundaries. A numerical validation of this technique on HF model has been provided. In ROM context, this approach simplifies POD implementation and avoids in particular interpolation issues related to the evaluation of inner products between fields defined on different domains and to the mapping of POD modes on deformed grids.

Third, the POD-Galerkin model has been extended via a new definition of time/space POD that gathers information from snapshot series around several profiles by means of a time/shape-averaging operator. In the present work, spatial POD modes are independent of shape parameter whereas POD temporal coefficients are shape-dependent. Airfoil deformation is captured in the ROM by a steady forcing term defined as the exact or approximated mean flow field. To approximate the forcing term, a linear actuation based on a 'deformation mode' has been considered as well as a quadratic interpolation approach.

Profile deformations that lead to significant modulations of POD temporal coefficients have been examined. ROM reliability towards airfoil parametrical deformation has been quantified. HF-resolved as well as unknown intermediate configurations are efficiently predicted by the ROM compared with HF simulations. This is particularly promising in the perspective of

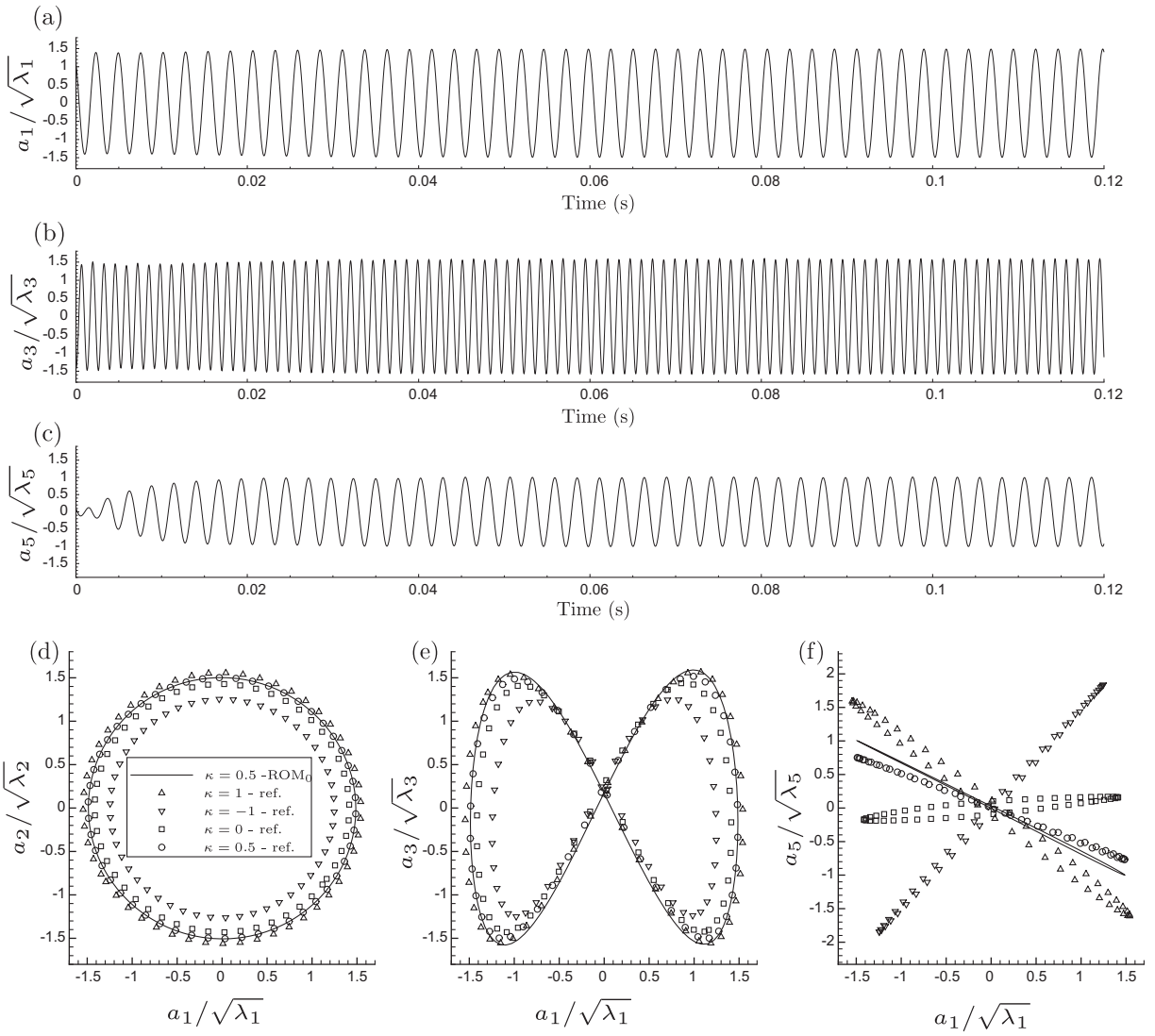

Fig. 26. Same as Fig. 14 in case $\kappa = 0.5$ where mean flow is approximated by $\hat{\boldsymbol{w}}_1$ (45).

the application of this low-dimensional modeling approach in optimal shape design procedures involving unsteady transonic flow simulations.

Acknowledgements

The authors gratefully acknowledge the referees for their helpful suggestions.

References

[1] K. Pearson, On lines and planes of closest fit to systems of points in space, Philos. Mag. 2 (1901) 559–572.
[2] K. Karhunen, Zur Spektraltheorie stochastischer Prozesse, Ann. Acad. Sci. Fenn. A1 34 (1946).
[3] J.L. Lumley, in: A.M. Yaglom, V.I. Tatarski (Eds.), Atmospheric Turbulence and Radio Wave Propagation, Nauka, Moscow, 1967.
[4] A. Deane, I. Kevrekidis, G.E. Karniadakis, S. Orszag, Low-dimensional models for complex geometry flows: application to grooved channels and circular cylinders, Phys. Fluids A 3 (10) (1991) 2337–2354.
[5] W. Cazemier, R.W.C.P. Verstappen, A.E.P. Veldman, Proper orthogonal decomposition and low-dimensional models for driven cavity flows, Phys. Fluids 10 (7) (1998) 1685–1699.
[6] X. Ma, G.E. Karniadakis, A low-dimensional model for simulating three-dimensional cylinder flow, J. Fluid Mech. 458 (2002) 181–190.
[7] B.R. Noack, K. Afanasiev, M. Morzynski, G. Tadmor, F. Thiele, A hierarchy of low-dimensional models for the transient and post-transient cylinder wake, J. Fluid Mech. 497 (2003) 335–363.
[8] B. Galletti, C.H. Bruneau, L. Zannetti, A. Iollo, Low-order modelling of laminar flow regimes past a confined square cylinder, J. Fluid Mech. 503 (2004) 161–170.

[9] B. Noack, P. Papas, P. Monkewitz, The need for a pressure-term representation in empirical Galerkin models of incompressible shear flows, J. Fluid Mech. 523 (2005) 339–365.
[10] M. Buffoni, S. Camarri, A. Iollo, M.V. Salvetti, Low-dimensional modelling of a confined three-dimensional wake flow, J. Fluid Mech. 569 (2006) 141–150.
[11] M. Couplet, C. Basdevant, P. Sagaut, Calibrated reduced-order POD-Galerkin system for fluid flow modelling, J. Comput. Phys. 207 (2005) 192–220.
[12] D.M. Luchtenburg, B. Günter, B.R. Noack, R. King, G. Tadmor, A generalized mean-field model of the natural and high-frequency actuated flow around a high-lift configuration, J. Fluid Mech. 623 (2009) 283–316.
[13] D. Venturi, X. Wan, G. Karniadakis, Stochastic low-dimensional modelling of a random laminar wake past a circular cylinder, J. Fluid Mech. 606 (2008) 339–367.
[14] D.J. Lucia, P.S. Beran, Projection methods for reduced order models of compressible flows, J. Comput. Phys. 188 (2003) 252–280.
[15] K. Hall, J. Thomas, E. Dowell, Proper orthogonal decomposition technique for transonic aerodynamic flows, AIAA J. 38 (10) (2000) 1853–1862.
[16] B.I. Epureanu, E.H. Dowell, K.C. Hall, Reduced-order models of unsteady viscous flows in turbomachinary using viscous-inviscid coupling, J. Fluids Struct. 15 (2001) 255–273.
[17] K. Willcox, J. Peraire, J. Paduano, Application of model order reduction to compressor aeroelastic models, J. Eng. Gas Turb. Power 124 (2) (2002) 332–339.
[18] J. Thomas, E. Dowell, K. Hall, Three-dimensional transonic aeroelasticity using proper orthogonal decomposition-based reduced-order models, J. Aircraft 40 (3) (2003) 544–551.
[19] T. Lieu, C. Farhat, Adaptation of aeroelastic reduced-order models and application to an F-16 configuration, AIAA J. 45 (6) (2007) 1244–1257.
[20] J. Thomas, E. Dowell, K. Hall, Using automatic differentiation to create a nonlinear reduced order model of a computational fluid dynamic solver, AIAA Paper 7115, 2006.
[21] C.W. Rowley, T. Colonius, R.M. Murray, Model reduction for compressible flows using POD and Galerkin projection, Physica D 189 (1–2) (2004) 115–129.
[22] G. Vigo, A. Dervieux, M. Mallet, M. Ravachol, B. Stoufflet, Extension of methods based on the proper orthogonal decomposition to the simulation of unsteady compressible Navier–Stokes flows, in: CFD'98, Proc. Fourth ECCOMAS Conf., Wiley, 1998, pp. 648–653.
[23] R. Bourguet, M. Braza, A. Dervieux, Reduced-order modeling for unsteady transonic flows around an airfoil, Phys. Fluids 19 (2007) 111704.
[24] W.R. Graham, J. Peraire, K.Y. Tang, Optimal control of vortex shedding using low-order models, Part I – open-loop model development, Int. J. Numer. Methods Eng. 44 (7) (1999) 945–972.
[25] W.R. Graham, J. Peraire, K.Y. Tang, Optimal control of vortex shedding using low-order models, Part II – model-based control, Int. J. Numer. Methods Eng. 44 (7) (1999) 973–990.
[26] S. Ravindran, A reduced-order approach for optimal control of fluids using proper orthogonal decomposition, Int. J. Numer. Methods Fluids 34 (2000) 425–448.
[27] M. Bergmann, L. Cordier, J.P. Brancher, Optimal rotary control of the cylinder wake using POD Reduced Order Model, Phys. Fluids 3 (2005) 1–21.
[28] P.A. Le Gresley, J.J. Alonso, Investigation of non-linear projection for POD based reduced order models for aerodynamics, AIAA Paper 0926, 2001.
[29] J.S.R. Anttonen, P.I. King, P.S. Beran, POD-based reduced-order models with deforming grids, Math. Comput. Model. 38 (1–2) (2003) 41–62.
[30] L.N. Sankar, S.Y. Ruo, J.B. Malone, Application of surface transpiration in computational aerodynamics, AIAA Paper 0511, 1986.
[31] M. Vázquez, B. Koobus, A. Dervieux, Multilevel optimisation of a supersonic aircraft, Finite Elem. Anal. Des. 40 (15) (2004) 2101–2124.
[32] C.L. Pettit, P.S. Beran, Reduced-order modeling for flutter prediction, AIAA Paper 1446, 2000.
[33] A. Bouhadji, Analyse physique par simulation numérique de phénomènes de transition bi-et tridimensionnels dans l'écoulement compressible, visqueux autour d'une aile d'avion, Ph.D. Thesis, Institut National Polytechnique de Toulouse, 1998.
[34] A. Bouhadji, M. Braza, Organised modes and shock-vortex interaction in unsteady viscous transonic flows around an aerofoil, Part I, Comput. Fluids 32 (9) (2003) 1233–1260.
[35] P.L. Roe, Approximate Riemann solvers, parameter vectors, and difference schemes, J. Comput. Phys. 43 (1981) 357–372.
[36] B. van Leer, Towards the ultimate conservative difference scheme. V. A second-order sequel to Godunov's method, J. Comput. Phys. 32 (1979) 101–136.
[37] C. Hirsch, Numerical Computation of Internal and External Flows, Computational Methods for Inviscid and Viscous Flows, vol. 2, Wiley, 1990.
[38] A. Bouhadji, M. Braza, Organised modes and shock-vortex interaction in unsteady viscous transonic flows around an aerofoil, Part II: Reynolds number effect, Comput. Fluids 32 (9) (2003) 1261–1281.
[39] J.B. McDevitt, L.L. Levy, G.S. Deiwert, Transonic flow about a thick circular-arc airfoil, AIAA J. 14 (5) (1976) 606–613.
[40] H.L. Seegmiller, J.G. Marvin, L.L. Levy, Steady and unsteady transonic flow, AIAA J. 16 (12) (1978) 1262–1270.
[41] G. Berkooz, P. Holmes, J.L. Lumley, The proper orthogonal decomposition in the analysis of turbulent flows, Ann. Rev. Fluid Mech. 25 (1993) 539–575.
[42] J.L. Lumley, A. Poje, Low-dimensional models for flows with density fluctuations, Phys. Fluids 9 (7) (1997) 2023–2031.
[43] L. Sirovich, Turbulence and the dynamics of coherent structures, Part I–III, Quart. Appl. Math. 45 (1987) 561–590.
[44] D. Rempfer, On low-dimensional galerkin models for fluid flow, Theor. Comput. Fluid Dyn. 14 (2) (2000) 75–88.
[45] N. Aubry, P. Holmes, J.L. Lumley, E. Stone, The dynamics of coherent structures in the wall region of a turbulent boundary layer, J. Fluid Mech. 192 (1988) 115–173.
[46] S. Sirisup, G.E. Karniadakis, A spectral viscosity method for correcting the long-term behavior of POD model, J. Comput. Phys. 194 (2004) 92–116.
[47] M. Bergmann, C.H. Bruneau, A. Iollo, Enablers for robust POD models, J. Comput. Phys. 228 (2) (2009) 516–538.
[48] A.N. Tikhonov, V.A. Arsenin, Solutions of Ill-posed Problems, Winston, Washington, 1977.
[49] L. Cordier, B. Abou El Majd, J. Favier, Calibration of POD reduced-order models by Tikhonov regularization, Int. J. Numer. Methods Fluids 63 (2) (2010) 269–296.
[50] R. Bourguet, M. Braza, A. Sévrain, A. Bouhadji, Capturing transition features around a wing by reduced-order modeling based on compressible Navier–Stokes equations, Phys. Fluids 21 (2009) 094104.
[51] J.S.R. Anttonen, P.I. King, P.S. Beran, Applications of multi-POD to a pitching and plunging airfoil, Math. Comput. Model. 42 (3–4) (2005) 245–259.
[52] M. Morzyński, W. Stankiewicz, B.R. Noack, F. Thiele, G. Tadmor, Generalized mean-field model with continuous mode interpolation for flow control, AIAA Paper 3488, 2006.
[53] C.S. Peskin, The immersed boundary method, Acta Numer. 11 (2002) 479–517.
[54] A. Dervieux, Perturbation deséquations d'équilibre d'un plasma confiné: comportement de la frontère libre,étude des branches de solutions, R.R. INRIA 0018, 1980.
[55] F. Beux, A. Dervieux, Extract-gradient shape optimization of a 2D Euler flow, Finite Elem. Anal. Des. 12 (1992) 281–302.
[56] A. Dervieux, Y. Mesri, F. Courty, L. Hascoet, B. Koobus, M. Vazquez, Calculs de sensibilité par différentation pour l'aérodynamique, in: ESAIM: Proceedings, vol. 22, 2007, pp. 181–189.
[57] J. Hadamard, Mémoire sur le problème d'analyse relatifà l'équilibre des plaquesélastiques encastrées, (1908), CNRS, Paris, 1968.
[58] P.R. Garabedian, Partial Differential Equations, Wiley, New York, 1964.
[59] E. Arian, M. Fahl, E.W. Sachs, Trust-region proper orthogonal decomposition for flow control, Icase Report 25, 2000.
[60] D. Amsallem, C. Farhat, Interpolation method for adapting reduced-order models and application to aeroelasticity, AIAA J. 46 (7) (2008) 1803–1813.
[61] M. Bergmann, L. Cordier, Optimal control of the cylinder wake in the laminar regime by trust-region methods and POD reduced-order models, J. Comput. Phys. 227 (2008) 7813–7840.
[62] E. Caraballo, C. Kasnakoğlu, A. Serrani, M. Samimy, Input separation methods for reduced-order model-based feedback flow control, AIAA J. 46 (9) (2008) 2306–2322.
[63] C. Kasnakoğlu, A. Serrani, M.O. Efe, Control input separation by actuation mode expansion for flow control problems, Int. J. Control 81 (9) (2008) 1475–1492.